Last edited: June 4, 2012
Preprint typeset using LaTeX style emulateapj v. 08/13/06

SHARDS: AN OPTICAL SPECTRO-PHOTOMETRIC SURVEY OF DISTANT GALAXIES

Pablo G. Pérez-González[1,2], Antonio Cava[1], Guillermo Barro[1,3], Víctor Villar[1], Nicolás Cardiel [1], Ignacio Ferreras[4], José Miguel Rodríguez Espinosa[5], Marc Balcells[5,6], Javier Cenarro[7], Jordi Cepa[5], Stéphane Charlot[8], Andrea Cimatti[9], Chris Conselice[10], Emmanuele Daddi[11], Jennifer Donley[12], David Elbaz[11], Néstor Espino[1], Jesús Gallego[1], R. Gobat[13], Rafael Guzmán[14], Alvio Renzini[15], Laurence Tresse[16], Ignacio Trujillo[5], Jaime Zamorano[1]

(Dated: Submitted: June 4, 2012)
Last edited: June 4, 2012

ABSTRACT

We present the Survey for High-z Absorption Red and Dead Sources (SHARDS), an ESO/GTC Large Program carried out with the OSIRIS instrument. SHARDS is an ultra-deep optical spectro-photometric survey covering the wavelength range between 500 and 950 nm with contiguous 24 medium-band filters (R∼50) and reaching magnitude 26.5 (3σ) and sub-arcsec seeing in all bands. SHARDS's main aim is obtaining accurate physical properties of intermediate and high-z galaxies using well-sampled optical SEDs with enough spectral resolution to measure absorption and emission features, whose analysis will provide reliable stellar population and AGN parameters. Among the different populations of high-z galaxies, SHARDS principal goal is characterizing in detail massive quiescent galaxies at z>1, whose existence is one of the major challenges of current hierarchical models of galaxy formation. In this paper, the basics about the survey observational strategy are presented, including a detailed discussion of the special reduction and calibration procedures which should be applied to the GTC/OSIRIS data, and the SHARDS data quality. We present preliminary results about the detection and study of emission-line galaxies (star-forming objects and AGN) at z=0–5. We also present and analyze the SEDs for high-z quiescent massive galaxies, discussing on the improvements introduced by the SHARDS dataset in the analysis of their star formation history.
CONCLUSION ABOUT READ AND DEAD GALAXIES

Subject headings: galaxies: starburst — galaxies: photometry — galaxies: high-redshift — infrared: galaxies.

1. INTRODUCTION

The current paradigm of galaxy formation establishes that the baryons closely follow the evolution of the Cold Dark Matter (CDM) halos, which cluster and grow hierarchically as shown in cosmological simulations and semi-analyticak models of galaxy formation, such as those in Springel et al. (2005, see also Baugh et al. 1998; Somerville & Primack 1999; Cole et al. 2000; Somerville et al. 2008; Ricciardelli & Franceschini 2010). In this scenario, star formation started within the cooling gas clouds in merging dark matter halos, after a slow early collapse regulated by feedback processes. This early star formation formed relatively small disk systems that later merged and formed larger (i.e., more massive) spheroidal systems (see, e.g., Kauffmann et al. 1993; Ellis et al. 2000, 2001)

MORE references in this last one sentence

The global picture about the co-evolution of matter in the Universe (including all graviting components: CDM and baryons) is self-consistent and has been successful in reproducing and even predicting many observables about galaxy evolution, especially at low redshift. Among the most relevant successes, we find the good comparison of models with the observed power spectrum of the Cosmic Microwave Background (Spergel et al. 2007; Komatsu et al. 2011) or the Large Scale Structure of the Universe (Percival et al. 2001; Colless et al. 2001). Also very convincing is the link between observations and theoretical expectations such as the existence and properties of the acoustic baryonic oscillations (Eisenstein et al. 2005; Gaztañaga et al. 2009; Percival et al. 2010). In addition, the current paradigm of a hierarchical scenario for

[1] Departamento de Astrofísica, Facultad de CC. Físicas, Universidad Complutense de Madrid, E-28040 Madrid, Spain
[2] Associate Astronomer at Steward Observatory, The University of Arizona
[3] UCO/Lick Observatory, Department of Astronomy and Astrophysics, University of California, Santa Cruz, CA 95064, USA
[4] Mullard Space Science Laboratory, University College London, Holmbury St Mary, Dorking, Surrey RH5 6NT
[5] Instituto de Astrofísica de Canarias, 38200 La Laguna, Tenerife, Spain
[6] Isaac Newton Group of Telescopes, Aptdo. 321, 38700 Santa Cruz de La Palma, Spain
[7] Centro de Estudios de Física del Cosmos de Aragón, Plaza San Juan 1, Planta 2, 44001 Teruel, Spain
[8] Institut d'Astrophysique de Paris, CNRS, Université Pierre & Marie Curie, UMR 7095, 98bis bd Arago, 75014 Paris, France
[9] Dipartimento di Astronomia, Universitá degli Studi di Bologna, I-40127 Bologna, Italy
[10] School of Physics & Astronomy, University of Nottingham, Nottingham NG7 2RD, UK
[11] CEA, Laboratoire AIM, Irfu/SAp, F-91191 Gif-sur-Yvette, France
[12] Space Telescope Science Institute, 3700 San Martin Drive, Baltimore, MD 21218, USA
[13] Laboratoire AIM-Paris-Saclay, CEA/DSM-CNRS-Université Paris Diderot, Irfu/Service d'Astrophysique, CEA Saclay, Orme des Merisiers, 91191 Gif-sur-Yvette, France
[14] Department of Astronomy, University of Florida, 211 Bryant Space Science Center, Gainesville, FL 32611, USA
[15] INAF - Osservatorio Astronomico di Padova, Vicolo dell'Osservatorio 5, I-35122 Padova, Italy
[16] Laboratoire d'Astrophysique de Marseille (UMR 6110), CNRS-Université de Provence, BP 8, 13376 Marseille Cedex 12, France

galaxy formation is also supported by the observations of galaxy mergers at different cosmological distances (e.g., van Dokkum et al. 1999; van Dokkum 2005; Miley et al. 2006), and the increase of the fraction of galaxies undergoing mergers as we move to higher redshifts (among others, Lacey & Cole 1993; Le Fèvre et al. 2000; Conselice et al. 2003; Bell et al. 2006; Lotz et al. 2008; López-Sanjuan et al. 2009).

The hierarchical galaxy formation scenario contrasts with several observational evidence, especially at high redshift (z>1–2), which favor a more classical monolithic collapse. This formation path was proposed 50 years ago to explain the formation of bulges such as the Milky Way's and spheroidal galaxies through a free-fall rapid collapse causing the formation of the bulk of the stars in these systems in a short period of time and then shutting off due to some *quenching* reason, leaving the galaxy to evolve passively (e.g., Eggen et al. 1962; Larson 1974). This theory was largely abandoned due, first, to the compilation of evidence that spheroidal galaxies suffer merging episodes (Toomre & Toomre 1972), and also that globular clusters and the general stellar population in the in the MW present a relatively wide range of ages (e.g., Searle & Zinn 1978), which directly points out to the hierarchical scenario. Then, the hierarchical picture was adopted instead due to the high degree of success of the ΛCDM models and semi-analytic models mentioned above.

However, rapid early episodes of intense star formation are indeed consistent (although not uniquely) with observational facts in nearby galaxies, such as the dominant old stellar populations in nearby bulges and ellipticals, their metallicity and α-elements enhancement, and the dynamics and shape of these systems (e.g., Vazdekis et al. 1997; Faber et al. 1997; Trager et al. 2000b,a). In addition, hierarchical models still present severe drawbacks in several aspects. The most challenging observational facts for hierarchical models refer to the lightest and heaviest galaxies. Indeed, hierarchical models typically present a "satellite problem", i.e., they predict many more low-mass galaxies than what is actually observed (see Kauffmann et al. 1993, 1999; Klypin et al. 1999; Kravtsov et al. 2004). On the bright end, models tend also to overpredict the number of massive galaxies observed in the local Universe, although they are getting closer to the observations after taking into account quenching mechanisms (Croton et al. 2006; De Lucia & Blaizot 2007; Somerville et al. 2008; Ricciardelli & Franceschini 2010).

The discrepancies between the predictions of current galaxy formation models based on the ΛCDM paradigm and the data are more obvious as we move to higher redshifts. In the last 15 years, a wide variety of papers using very heterogeneous data and methods have presented compelling evidence that the formation of galaxies follows a so-called *downsizing* scenario (Cowie et al. 1996; Heavens et al. 2004; Glazebrook et al. 2004; Bauer et al. 2005; Pérez-González et al. 2005; Arnouts et al. 2007; Pérez-González et al. 2008). In this theory, the most massive galaxies formed first in the history of the Universe, thus having the oldest stellar populations seen today. The formation of less massive systems continued at lower redshifts. Downsizing implies that most of the star formation in the most massive galaxies happened quick and stopped for some reason in early times. This also means that there should be massive passively evolving galaxies at high redshift. This kind of objects have indeed been detected at redshifts around z∼1–3 with a variety of techniques (Yan et al. 2000; Franx et al. 2003; Daddi et al. 2004; Papovich et al. 2006; Cimatti et al. 2008).

The finding of massive galaxies at z=1–3, some of them already evolving passively, is indeed extremely challenging for current models of galaxy formation based on the ΛCDM matter paradigm, which predict many less massive systems at high-z than observed (see, e.g., Marchesini et al. 2009; Henriques et al. 2012; Leauthaud et al. 2012). Indeed, the downsizing scenario contradicts, at least at first sight, the predictions of a hierarchical assembly of the stellar mass in galaxies, i.e., the most massive galaxies do not seem to be the result of multiple mergers occurring in a extended period along the Hubble time (Baugh et al. 1998; Cole et al. 2000; Faber et al. 2007). Still, a hierarchical assembly with (maybe multiple) mergers occurring at high redshift between gas-rich systems (a process close in nature to a monolithic collapse) would be consistent with the downsizing evidence and the properties of the dominant stellar populations seen in nearby spheroidal systems.

Our understanding of the processes involved in the early (z>1) assembly of galaxies (and also the evolution from the early Universe to the present) is still hampered by the significant (often systematic) uncertainties in our estimations of their physical properties. Our global picture of the galaxy formation will only improve if we are able to get more robust estimations of some key properties of galaxies, such as the stellar masses, SFRs, and extinctions. Jointly with those, we of course need better estimations of the distances to galaxies based on spectroscopic or photometric redshifts, which can be used to relate the mentioned galaxy properties with other relevant parameters such as the environment. The improvements in the determination of stellar masses and SFRs/extinctions will also mean a better estimation of the age of the stellar population and the Star Formation Histories, SFH (see, e.g, Papovich et al. 2001; Fontana et al. 2006; Kriek et al. 2008; Elsner et al. 2008; Pforr et al. 2012). Jointly with this observational effort, we will need better physics in the models, which should give us, for example, more certain emissivities of the stellar populations in the rest-frame NIR, now effected by strong uncertainties due to the little known about the properties and importance of stellar evolutionary phases such as the thermally-pulsating TP-AGB phase (see Maraston 2005; Kriek et al. 2010). The task of obtaining more robust physical parameters of galaxies at cosmological distances is even more interesting for those massive galaxies already quiescent and evolving passively at high-z, whose number densities and properties are the most demanding challenges of current galaxy evolution models. The cosmological importance of these systems is very high, since they most probably represent the early formation phases of present-day early-type galaxies.

In this paper, we presented the basics of the *Survey for High-z Absorption Red and Dead Sources* (SHARDS), an ESO/GTC Large Program awarded with 180 hours of GTC/OSIRIS time during 2010-2013. This project consists of an ultra-deep (m<26.5 mag) imaging survey in

24 medium-band filters covering the wavelength range between 500 and 950 nm and targeting the GOODS-N field. The data acquired by SHARDS allow to accurately determine the main properties of the stellar populations present in these galaxies through spectro-photometric data with a resolution R∼50, typically enough to measure absorption indices such as the D(4000) (e.g., Bruzual A. 1983; Balogh et al. 1999; Kauffmann et al. 2003a; Kriek et al. 2011) or Mg(UV) index (Spinrad et al. 1997; McCarthy et al. 2004; Saracco et al. 2005; Daddi et al. 2005b; Cimatti et al. 2008). The analysis of these spectral features is a powerful method to constrain the solution of stellar population synthesis models and improve our estimations of parameters such as the age, SFH, mass and extinction of galaxies at cosmological distances.

SHARDS inherits the observational strategy of optical surveys such as COMBO17 (Wolf et al. 2001, 2003), the COSMOS medium-band survey (Ilbert et al. 2009), ALHAMBRA (Moles et al. 2008), or PAU/J-PAS (Benítez et al. 2009a; Abramo et al. 2011). These projects have demonstrated the impact of large photometric datasets on our understanding of the formation of galaxies (see, among many papers, Bell et al. 2004; Faber et al. 2007; Wolf et al. 2004; Rix et al. 2004; Borch et al. 2006; Caputi et al. 2006; Scoville et al. 2007; Benítez et al. 2009b; Cardamone et al. 2010; Whitaker et al. 2011). SHARDS intends to be a step forward from these surveys in terms of depth, spectral resolution, and data quality. Our survey prioritizes the detailed study of the faintest galaxies at the highest redshifts over the analysis of closer galaxy populations and the Large Scale Structure at intermediate redshift, and thus focuses on a smaller area than the surveys mentioned above. Indeed, SHARDS was planned to reach up to 3 mag fainter than those surveys, uses typically twice the number of filters in the same wavelength range (i.e., our spectral resolution is better), and was obtained in magnificent (sub-arcsec) seeing conditions with a 10m class telescope. In contrast, it covers a fraction of the area surveyed by other projects.

In this paper, we present the main technical characteristics of the survey in Section 2, including a thorough discussion of the reduction and calibration procedures in Section 3. Next, we present our science verification results about emission-line and absorption systems. In Sections 4.1 and 4.2, we discuss about the capacity of the SHARDS data to select and study emission-line sources (star-forming galaxies and AGN) at intermediate and high redshifts (from z∼0 to z∼5 and beyond). In Section 5, we present detailed spectral energy distributions of massive quiescent galaxies at z>1, and demonstrate the power of our spectro-photometric data to analyze the stellar populations in this kind of objects through detailed comparison with stellar population synthesis models.

Throughout this paper we use AB magnitudes. We adopt the cosmology $H_0 = 70$ km^{-1}s^{-1}Mpc^{-1}, $\Omega_m = 0.3$ and $\Omega_\lambda = 0.7$.

2. SURVEY DESCRIPTION

The Survey for High-z Absorption Red and Dead Sources (SHARDS) is a medium-band optical survey currently being carried out with the Spanish 10.4m telescope, GTC, and its OSIRIS instrument. SHARDS was approved in 2010 as an ESO/GTC Large Program and awarded with 180 hours of observing time to obtain data through contiguous 24 medium-band filters covering the wavelength range between 500 and 950 nm and targeting the GOODS-N field. SHARDS was conceived to analyze in detail the properties of the stellar populations in 0<z<4 galaxies (and beyond), focusing especially in the analysis of quiescent massive galaxies at z=1.0–2.5. To achieve this goal, the survey was planned to obtain photometric data in as many filters as necessary to cover the entire optical window with enough spectral resolution to be able to measure reliably absorption indices which could be used to perform a detailed and robust stellar population synthesis. Given that spectral indices, such as D(4000) or Mg(UV), use spectral windows of around 100-200 nm, SHARDS' filters were built to have that spectral resolution at z>1, thus imposing widths of around 17 nm. The brightness of the night sky at wavelengths beyond ∼800 nm, implies that filters as narrow as 17 nm would not reach the needed magnitude limit to study high-z sources, so our 2 reddest filters are twice as wide. SHARDS was conceived to reach the typical magnitudes of L* galaxies at z>1 for every single filter, so the goal was to obtain a depth of 26.5-27.0 mag at the 3σ level with sub-arcsec seeing. The final manufacturing process of the filters resulted in an average width for our filter set around 15-16 nm, except for the 2 reddest filters, which have a width around 33-35 nm. Figure 1 shows the layout of the filter set and the observational strategy of SHARDS. The characteristics of the filters are given in Table 1, jointly with other details of the SHARDS data.

SHARDS is being carried out in the GOODS-N field, one of the most targeted areas of the sky at all wavelengths. Virtually all the region covered by ACS is be-

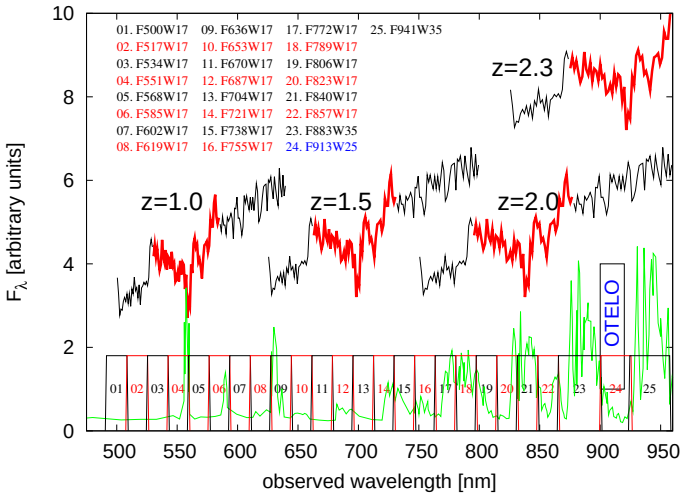

FIG. 1.— Observing strategy of SHARDS. We show how the stacked spectrum of the 13 spectroscopically confirmed quiescent massive galaxies at 1.4<z<2.0 in GOODS-S (Cimatti et al. 2008, the stack adds up 480 hours of VLT time) would look like at 4 different redshifts, together with the profiles of the SHARDS filter system. The sky spectrum is also depicted in green. Using 24 filters (FWHM∼17 nm), SHARDS is able to probe the prominent absorption feature placed at λ=265295 nm, distinctive of passively evolving galaxies (marked in red) with a resolution R∼50, measure it strength with a spectro-photometric technique, and accurately measure stellar ages, or distances for individual high-z galaxies. The 900 nm atmospheric window is not covered by our survey, since it will be covered by another approved GTC Guaranteed Time project (OTELO, Cepa et al. 2011; Lara-López et al. 2011).

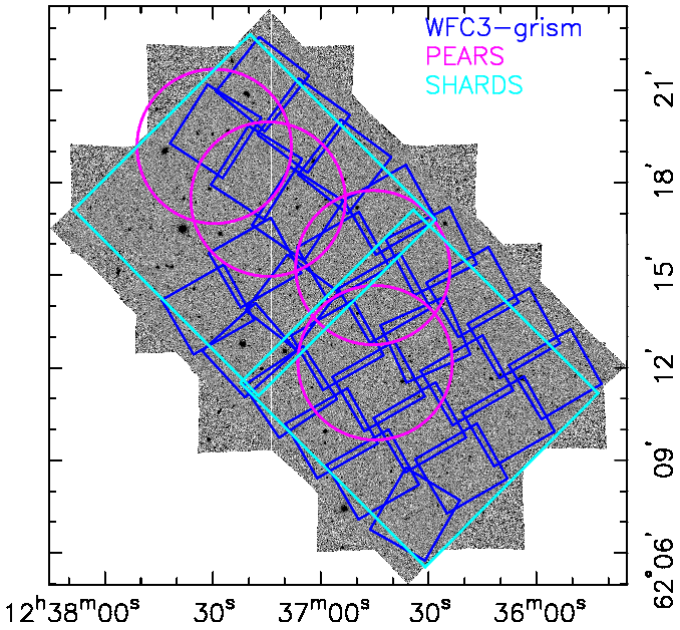

FIG. 2.— Footprint of the SHARDS data overimposed on the ACS images from GOODS. The footprints of the HST grism surveys carried out with ACS (PEARS) and WFC3 (PI: Weiner) are also shown.

ing surveyed by SHARDS using two OSIRIS pointings, summing up a total surveyed area of ∼135 arcmin^2 (see Figure 2). The multi-wavelength dataset available in GOODS-N is extensive, ranging from an ultra-deep X-ray exposure to the deepest data in the MIR/FIR with surveys such as FIDEL (Frayer et al. 2006), PEP (Lutz et al. 2011), HerMES (Oliver et al. 2010), or Herschel-GOODS (Elbaz et al. 2011), as well as multiple spectroscopic redshifts (Wirth et al. 2004; Cowie et al. 2004; Reddy et al. 2006), a few of them at z>1.5 (Reddy et al. 2005; Barger et al. 2008). Very complementary to the SHARDS data, GOODS-N counts with intermediate resolution spectroscopy obtained with HST (see Figure 2) in the optical (PEARS, Kümmel et al. 2009; see also Pirzkal et al. 2004, 2009) and NIR (PI: B. Weiner). In addition, the availability of the sky deepest IRAC ([3.6]<26.0 mag) and MIPS [F(24)>15 μJy] observations ensures the detection of the rest-frame NIR/MIR emission of the galaxies and allow us to robustly estimate stellar masses and SFRs (Pérez-González et al. 2005, 2008; Cimatti et al. 2008). Also noticeable is the availability of the deepest Herschel PACS survey through an Open Time Key Program (Herschel-GOODS; Elbaz et al. 2011). This wealth of data converts GOODS-N in one of the two best regions in the sky for the study of the first galaxies and their evolution, and the best in the Northern sky Hemisphere.

CANDELS footprint

At the time of publication of this paper, 75% of the SHARDS data have already been taken. Table 1 presents the data characteristics for the observed pass-bands in both SHARDS pointings.

3. DATA REDUCTION AND CALIBRATION

3.1. *Reduction pipeline*

The GTC/OSIRIS instrument (Cepa 2010) is an optical imager equipped with 2 CCDs, which cover a total (usable) field-of-view of 7.4′×8.4′. There is a gap between the 2 detectors, with size 10–12″ as measured directly in our images in different locations along the gap and after masking non-useful pixels and correcting for distortions. OSIRIS presents special characteristics which should be taken into account in the data reduction procedure. Indeed, apart from the standard reduction steps (bias subtraction and flat-fielding), our custom OSIRIS pipeline includes the following additional steps: illumination correction, background gradient subtraction, fringing removal, WCS alignment taking into account field distortions, and 2-dimensional calibration of the photometric pass-band and zeropoint. We describe these steps in detail in the following paragraphs, carefully describing the non-standard parts of the reduction.

Bias frames were taken each night. These calibration data were found to be very stable and uniform, with typical variations of less than 3% from pixel to pixel and from night to night. Dark current was found to be negligible in all our data.

Sky flats for each filter in the SHARDS dataset were taken at sunset and dawn every night. These flats presented strong gradients across the field (typically, 10-50% differences in brightness from one edge of the FOV to another), with significant spatial and temporal brightness variations. These gradients were also seen in science data during both dark and (especially) gray night time.

After analyzing night and day-time data, we concluded that these spatial variations were mainly due to the special characteristics of the OSIRIS instrument, which operates off-axis for our observational setup (medium- and broad-band imaging). Indeed, light rays reach the OSIRIS detector (when not using the tunable filters) in a wide range of angles of incidence (AOI): –2°<AOI<22°. Given the typical dependence with the light ray's AOI of the central wavelength (CWL) of the passband for interference filters, and the medium-width of our filter set, our flat-field frames were subject to the spectral features of the sky spectrum, and its temporal variations.

The optical axis is outside the OSIRIS FOV when using a single broad- or medium-band filter. For this reason, a gradient is observed in our data (flat-field and science images), with a symmetry around an horizontal line approximately dissecting in equal parts the FOV in the vertical direction. The gradient follows a radial profile centered in the optical axis. It presents varying structures of different brightnesses whose position and strength depend on time and the actual filter used. The brightest structures are located where strong sky emission lines (or bands) go through the pass-band for each physical filter as its CWL is changing along the FOV.

This effect directly related to the special characteristics of OSIRIS and our instrumental setup means that it is very difficult to find a spatially constant light source to take flat-fields, i.e., a significant part of the structure of the flat-field frames is linked to the sky spectrum. Thus, our pipeline included an illumination correction to get rid of this effect as much as possible. This illumination correction was carried out by comparing the flat-field images taken for our medium-band filters with those acquired through broad-band pass-bands (typically, r- and i-band filters). For these broad-band filters, the sky spectrum

is averaged in a wide enough spectral range that they do not show strong spatial variations, and are also very constant in time. Indeed, the super-skyflat provided by the observatory and built with thousands of frames show variations of less than 5% along the FOV and from night to night.

We used the ratio of our medium-band flat-fields to the broad-band flat-fields to correct the SHARDS data for illumination correction. These ratios were smoothed using a $3^{\rm th}$-order spline.

After applying the flat-field and illumination corrections to the science data, these images presented a highly symmetric sky gradient, which was subtracted with a spline interpolation and median filtering, after masking objects. In order to avoid the effect of the wings of the objects in this sky determination, we increased the extension of the sources (typically by a factor of 2 in radius) taking into account their brightnesses, and we also masked faint objects which were detected in a preliminary mosaic constructed for each filter adding all the available data.

The data for the filters whose CWL is redder than ∼700 nm presented some fringing (typically with an intensity below 1%). We removed this additive effect using the RMFRINGE task in IRAF.

Before stacking all the data together, we calibrated the World Coordinate System (WCS) for each image using the positions of several hundred objects for each CCD, which were cross-correlated with a sample of galaxies detected in the Subaru *R*-band image of GOODS-N. For this task, we used the SCamp program, and the WCS utilities in IRAF, obtaining for each frame an undistorted image remapped to a TAN-SIP coordinate system. The distortion in individual frames reaches several arcseconds in the edges, and the final WCS calibrated images present a typical position uncertainty around 0.1″throughout the FOV.

Finally, the SHARDS pipeline stacks together all the data for a given filter with a sigma-clipping algorithm to get rid of cosmic rays and artifacts, producing final mosaics and exposure maps with the same WCS for all SHARDS filters and for each of our 2 pointings covering the GOODS-N field.

3.2. *Calibration procedures*

Given the special characteristics of the OSIRIS instrument at GTC, within each single frame taken with a given physical filter, each pixel sees a different pass-band. This has a strong effect on the images taken with medium-band filters, where the shift of the central wavelength of the actual filter seen by different parts of the detector produces sky gradients and significant difficulties in obtaining flat-field calibration images, as explained in the previous section. This translates to the need of calibrating the SHARDS data in two different aspects: calibration of the pass-band and determination of the photometric zeropoint, both as a function of the position in the FOV. Although part of the spatial variation of the photometric zeropoint can be removed with an illumination correction built with broad-band flat-field images, a small effect can remain in the images, so we tried to measure it during our calibration procedure. After this calibration, we would be able to obtain a photometric catalog for each physical filter, but within this catalog

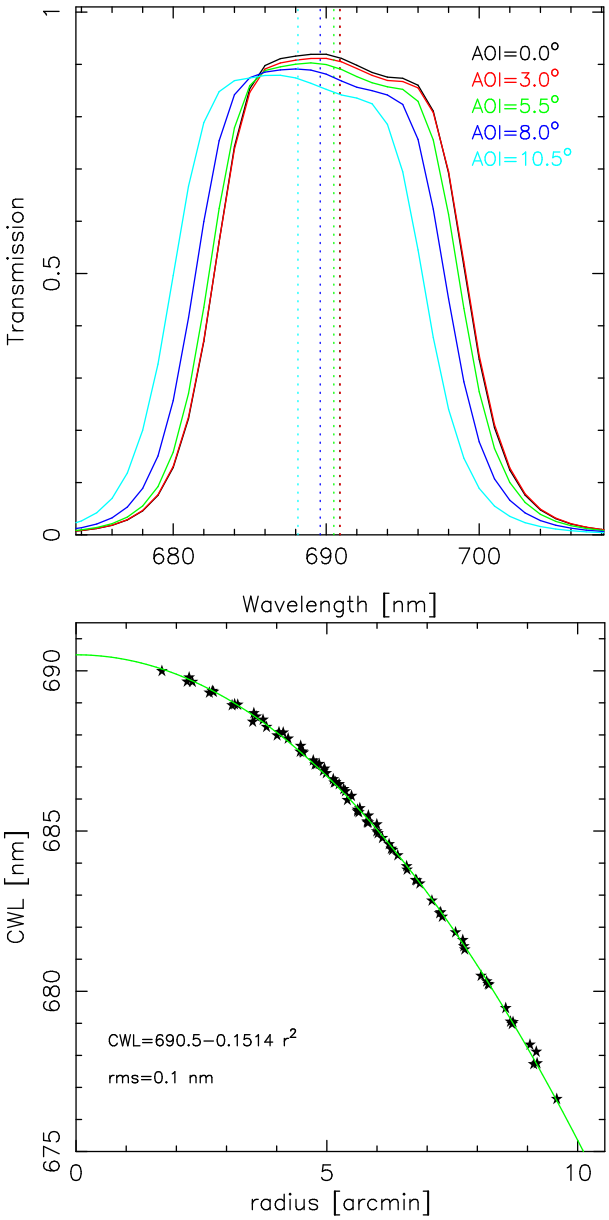

FIG. 3.— *Top:* Calibration of the transmission curve of the F636W17 filter as a function of angle-of-incidence (AOI), obtained with laboratory data. The central wavelengths (CWL) of each pass-band are marked with vertical lines. *Bottom:* Calibration of the spatial variation of the CWL of the F636W17 filter along the OSIRIS FOV. The data are fitted with the function in Equation 1, leaving the position of the optical axis as a fitting parameter.

the flux measurements for each detected source will refer to a different pass-band. We describe the procedures to carry out the calibration of the SHARDS data in the following subsections, starting from the CWL calibration and following with the absolute flux calibration.

3.2.1. *Pass-band central wavelength (CWL) calibration*

The dependence of the central wavelength (CWL) of the pass-band seen by different parts of the OSIRIS detector for a given physical filter was calibrated with daytime imaging and spectroscopic data taken in laboratory and at GTC. In the lab, we calibrated the transmission curve for each filter as a function of the angle-of-incidence

TABLE 1
CHARACTERISTICS OF THE SHARDS FILTER SET AND OBSERVATIONS (BEFORE 2012A).

Filter	CWL[a]	Width	A	B	X_0	Y_0	rms	ΔZP		$m_{3\sigma}$		$m_{75\%}$		seeing	
								P1	P2	P1	P2	P1	P2	P1	P2
(1)	(2)	(3)	(4)	(5)	(6)	(7)	(8)	(9)	(9)	(10)	(10)	(11)	(11)	(12)	(12)
F619W17	618.9	15.1	623.14	-2.402e-6	-202	985	0.10	0.077	···	26.89	···	27.22	···	0.85	···
F636W17	638.4	15.4	641.37	-2.587e-6	-116	986	0.10	0.066	0.072	26.78	26.70	27.15	27.17	0.79	0.92
F653W17	653.1	14.8	656.01	-2.634e-6	-151	999	0.10	0.063	0.065	26.91	27.07	27.17	27.15	0.98	1.00
F670W17	668.4	15.3	671.86	-2.600e-6	-183	1037	0.10	0.062	0.064	26.64	26.76	27.12	27.18	0.79	1.07
F687W17	688.2	15.3	690.50	-2.674e-6	-186	983	0.10	0.050	0.055	27.04	26.85	27.10	27.09	0.84	0.93
F704W17	704.5	17.1	707.78	-2.723e-6	-209	1028	0.10	0.055	0.063	26.71	26.63	27.01	26.95	0.89	0.92
F721W17	720.2	18.2	723.12	-2.969e-6	-94	960	0.10	0.056	0.060	26.60	26.51	26.97	26.96	0.93	1.02
F738W17	737.8	15.0	741.80	-2.411e-6	-328	1050	0.10	0.050	0.061	26.45	26.25	26.95	26.87	0.86	0.90
F755W17	754.5	14.8	758.12	-2.660e-6	-228	1034	0.10	0.050	0.055	26.69	26.37	26.93	26.91	0.92	0.93
F772W17	770.9	15.4	774.62	-2.929e-6	-122	1026	0.10	0.054	0.053	26.54	26.34	26.90	26.83	0.94	1.04
F789W17	789.0	15.5	791.22	-3.087e-6	-123	994	0.10	0.054	0.056	26.22	26.02	26.84	26.63	0.97	0.92
F806W17	805.6	15.6	809.42	-2.939e-6	-200	933	0.10	0.051	0.050	26.39	26.38	26.82	26.77	0.96	0.99
F823W17	825.4	14.7	829.15	-3.055e-6	-153	888	0.10	0.049	0.049	26.59	26.65	26.91	26.89	0.82	0.91
F840W17	840.0	15.4	843.51	-3.103e-6	-237	992	0.10	0.057	0.056	26.13	26.19	26.79	26.74	0.88	0.91
F857W17	856.4	15.8	859.97	-2.892e-6	-249	1002	0.10	0.050	0.051	26.84	26.23	26.88	26.63	0.73	0.95
F883W35	880.3	31.7	885.33	-2.889e-6	-285	978	0.10	0.065	0.057	26.06	26.06	26.64	26.58	0.93	1.02

NOTE. — (1) Filter name. (2) Central wavelength (in nm) of the filter for angle of incidence AOI=10.5° (approximately that for the center of the FOV). (3) Filter width (in nm). (4) Coefficient A (in nm) for CWL calibration (from equation 1). (5) Coefficient B (in pixel^{-2}) for CWL calibration (from equation 1). (6) X coordinate for the OSIRIS optical center (in pixels). (7) Y coordinate for the OSIRIS optical center (in pixels). (8) RMS of the CWL calibration (in nm). (9) Zeropoint uncertainty for pointings 1 and 2. (10) Sensitivity limit at 3-σ level (AB mag) for pointings 1 and 2. (11) Third quartil of the magnitude distribution (AB mag) for pointings 1 and 2. (12) Average seeing (in arcsec) for pointings 1 and 2.

of the incoming beam. At the telescope, once the filter were mounted in OSIRIS, we took spectroscopic data through a special mask with 105 pinholes homogeneously covering the entire FOV. The positions of those pinholes were determined in images taken through the mask and one of our filters. Then we also took spectra of these pinholes with the R1000B and R1000R grisms (which cover the entire wavelength range probed by SHARDS) through our filters, calibrating them with Ne, HgAr, and Xe arcs. Typical uncertainties in the wavelength solution were smaller than 0.01 nm. These data were used to measure the transmission curve at each pinhole position. Then, we analyzed each curve determining the CWL and width of the pass-band seen by each pinhole. We found negligible (less than 0.2 nm) differences of the width of the pass-bands and shape of the pass-band from one pinhole to any other, but a significant symmetric variation of the CWL around the optical axis, located to the left of the FOV. The CWLs for all the pinholes were fitted with a r^2 function, leaving also the position of the optical axis as a parameter to fit. An example of the calibration for one of the SHARDS filters is shown in Figure 3. The data were fitted with the following function:

$$CWL(X,Y) = A + B \times \sqrt{(X - X_0)^2 + (Y - Y_0)^2} \quad (1)$$

where X and Y are the positions (in pixels) in the OSIRIS FOV, and X_0 and Y_0 are the position of the optical axis, combined all of them to give a distance to the optical axis in pixels. X_0, Y_0, A,and B were measured for each one of the SHARDS filters. When applied to the actual science data, the optical axis position was converted to RA and DEC, and the distances were measured in arcmin using the nominal pixel size of our data, 0.251 arcsec/pixel.

The fitting coefficients in Equation 1 for each one of the SHARDS filters are given in Table 1.

Example of CWL calibration in real data: nearby galaxy. Or leave for Science demonstration or for Antonio's paper.

3.2.2. *Photometric calibration*

The significant variation of the passband seen by each galaxy as a function of position in the FOV implies a complex behavior of the absolute photometric calibration of the SHARDS images. Moreover, the effects of this CWL variation on the construction of the flat-field (explained in Section 3.1) may also affect the flux calibration of the final mosaics. To cope with these issues, we developed a special flux calibration procedure, aimed at determining the flux calibration of the SHARDS mosaics in each filter as a function of position in the image. Alternatively, since the behavior of the passband is symmetric around the optical axis and each position in the FOV is characterized by a central wavelength (as explained in Section 3.2.1 and defined by Equation 1), we refer the photometric calibration to CWL values seen by each position in the FOV, instead of directly relating the calibration to a position in the images.

The primary flux calibration of the SHARDS mosaics was performed by comparing the measured photometry in our images with spectroscopic data. Synthetic fluxes were obtained by convolving spectra for several sources in the field with the appropriate transmission curve seen by that source, according to our calibration of the passband (see Section 3.2.1). The spectra used in this calibration procedure were taken from 2 different sources: (1) the HST ACS grism data for compact galaxies from the PEARS project (Ferreras et al. 2009); and (2) the spectroscopic data released by the Keck Team Redshift Survey (Wirth et al. 2004) and DEEP3 (Cooper et al. 2011) taken with the Keck/DEIMOS instrument. Given that the TKRS and DEEP3 spectra are not flux calibrated, they are not completely flat-fielded in the spectral direction (see below), and are subject to the effect of strong sky emission lines and telluric absorption bands in certain spectral regions, our primary calibrator is the PEARS dataset of HST/ACS spectra. The Keck spectra

are used as a consistency check for the primary calibration. In addition, we also performed another test of the calibration based on synthetic magnitudes obtained from stellar population models fitting the broad band photometry for the galaxies with a published spectroscopic redshift and compiled in the Rainbow Cosmological Surveys database (see Pérez-González et al. 2008; Barro et al. 2011a,b). A finer calibration will be carried out in the future based on high SNR (SNR>10) spectra for bright objects which are currently being obtained at TNG and the CAHA 3.5m telescope.

The basic calibration procedure starts with a crude determination of the zeropoint based on the comparison of photometry in the SHARDS images with R- or I-band fluxes. This comparison provides a first estimation of the conversion from counts to AB magnitudes. Then, the main part of the calibration procedure consists in scaling the HST ACS grism spectra of compact sources extracted from Ferreras et al. (2009) and high-SNR spectra downloaded from the PEARS database[17] to the broad-band photometry in the *viz* bands from ACS. The flux measurement in the ACS bands is carried out at a large enough aperture so it can be compared with photometry in the SHARDS images with negligible seeing effects and also avoiding the contamination of nearby sources. Typically, apertures with radii larger than $1''$ were used. The procedure basics are outlined in Figure 4.

Figure 5 shows the results of the calibration based on HST/ACS spectra. We plot the offset between the calibration obtained from the analysis of the HST spectra and the preliminary calibration obtained with the comparison with I-band fluxes as a function of the CWL of the passband seen by each galaxy. In this example, we show the results for the observations of one of the SHARDS pointings through the F636W17 filter, where we count with more than 1,500 ACS spectra to compare. In the case of the second pointing, PEARS only covered a part of it, and the number of available ACS spectra is ∼900. The derived differential calibration as a function of wavelength (i.e., position) was applied to the images, so the final mosaics have a constant zero-point throughout the whole image. The typical scatter around the average calibration is 0.05 mag.

The calibration obtained with the HST data was checked with other spectra found in the literature. We found nearly 1,000 spectra for sources detected by SHARDS in the TKRS database and the DEEP3 release in GOODS-N (Wirth et al. 2004; Cooper et al. 2011). The spectra were all taken with the DEIMOS instrument on Keck with typical exposure times of 1-2 hours through R∼300–600 grisms. Given that these surveys were mainly interested in spectroscopic redshifts based on emission-lines, the typical SNR in the continuum is low (SNR∼1 at the original spectral resolution of 0.1 nm). In addition, the spectra are not flux calibrated and they typically show a decrease of flux to the blue that seems to arise from the lack of an accurate spectral flat (see Figure 6). For these reasons, we just used these spectra as a test for our basic absolute flux calibration based on HST data. Prior to this test, we had to correct the individual ground-based spectra with an average spectral flat and flux calibrate them. Both procedures were carried out using broad-band photometry and fits to this photometry with stellar population synthesis models from the Rainbow Cosmological Surveys database (Pérez-González et al. 2008).

Figure 6 shows a typical spectrum in GOODS-N extracted from the TKRS database and DEEP3 data release. After binning the spectrum to a resolution of 2 nm, we carried out a preliminary flux calibration of the spectrum based on the photometric broad-band data around 800 nm (blue stars in the right panels of the figure). An inspection of the resulting calibrated spectra (thick black lines in Figure 6) revealed that the spectroscopic data were not corrected with an adequate spectral flat, resulting in a large and increasing flux difference between the spectra and the broad-band photometric data at shorter wavelengths (see comparison between black thick lines and the photometry in Figure 6). To correct for this effect, we built a master spectral flat by averaging the comparison between all the available spectra and stellar population synthesis models fitting the broad-band photometry (red lines in Figure 6). After applying this correction, the comparison between the spectra (thin black lines in Figure 6) and the photometry was better, but still most sources presented a dimmer flux level in the spectra when compared with the photometry. We identified this flux difference as an effect of differential extinction, which was not fully taken into account in the average spectral flat. To account for this, we applied a final correction based on a typical extinction curve at Mauna Kea scaled to account for the difference between the spectra and the broad-band photometry (especially in the bluest bands). This final spectrum (green lines in Figure 6) was then convolved with the SHARDS filter pass-band (the appropriate one according to the position of the galaxy in the FOV), providing another independent calibration for our data.

Finally, the fluxes obtained in the SHARDS band were compared directly with synthetic magnitudes obtained by convolving the SHARDS filter pass-bands with stellar population synthesis models fitting the broad-band photometry for each source. Note that this calibration test is not completely independent of the one carried out with the ground-based spectra since these spectra were partially calibrated with the stellar population fits. Moreover, the comparison with models for individual galaxies may be biased due to the presence of emission-lines, which are not constrained by the broad-band photometry. However, templates count with a lower noise and we have the possibility to compare with a large number of galaxies, since even the fits for galaxies with no spectroscopic redshift could be reliable in a statistical way since our convolutions with the SHARDS filters are interpolations between broad-band fluxes. Therefore, the comparison with the templates is another good test of the absolute flux calibration, and it indeed provided reassuring results for all filters.

QUANTIFY EVERYTHING

In summary, the flux calibration of the SHARDS data was based on the comparison with a combination of HST/ACS grism spectra, ground-based spectra, and stellar population synthesis models fitting the broad-band photometry. Based on this calibrators, we estimated the typical uncertainty in the zeropoints of the SHARDS im-

[17] http://archive.stsci.edu/prepds/pears/

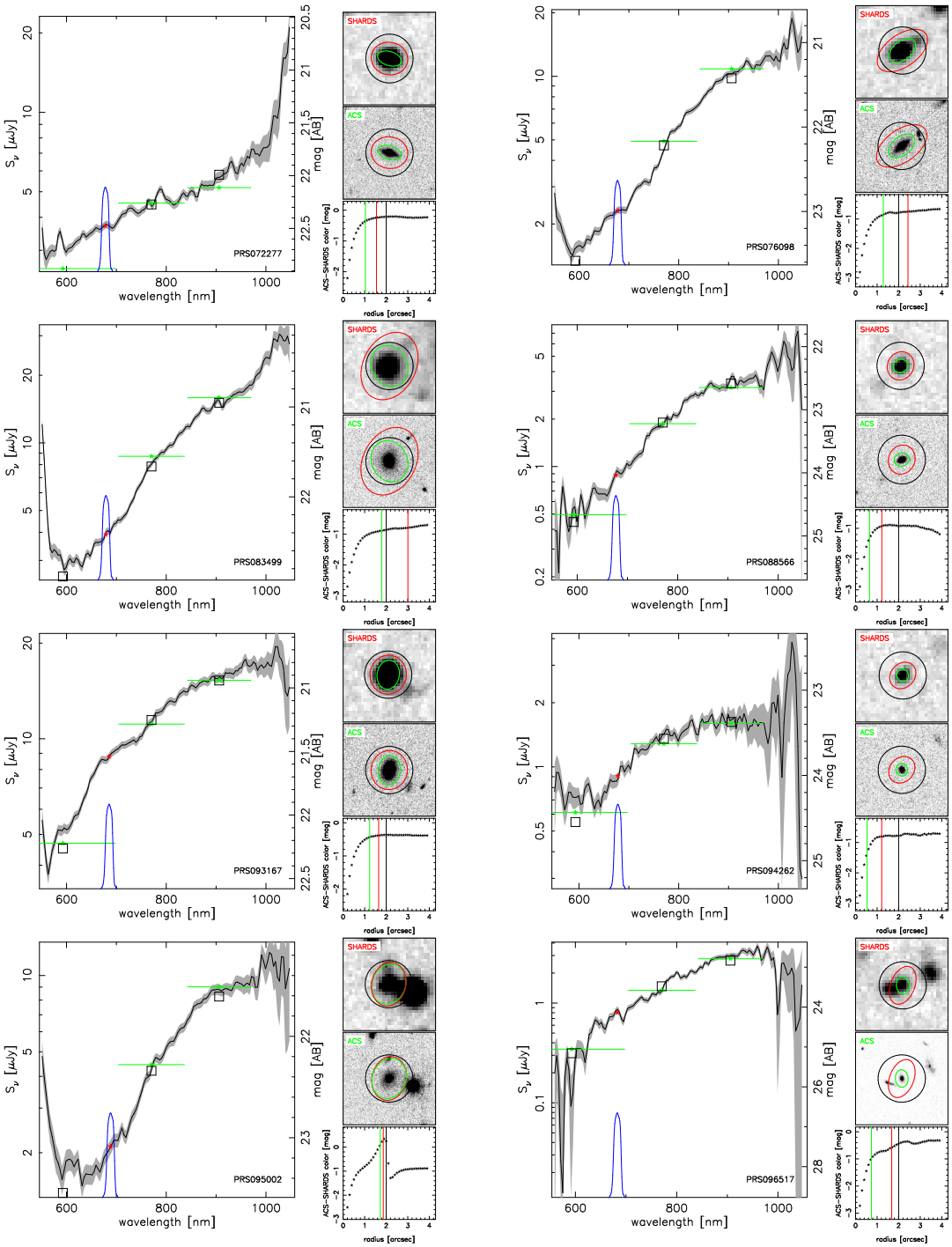

FIG. 4.— Examples of the HST/ACS spectra (from the PEARS data described in Ferreras et al. 2009 and the PEARS database) used in the calibration of the SHARDS data. The figure shows the results for one of the two SHARDS pointings through the filter F687W17, where we count with more than 1,500 comparison objects. The ACS spectra are shown in black with the gray shaded area depicting the uncertainties. The spectra are scaled to the ACS *viz* photometry, shown in green, including also uncertainties and filter widths. The convolution of the spectra with the *viz* filter transmission is shown with squares. The passband for the F687W17 filter seen by each galaxy is shown in blue, and the convolution with the HST spectra is marked with a red star. Jointly with each spectrum, we show the SHARDS and i-band ACS images of the galaxy ($5'' \times 5''$) and the color between them as a function of aperture radius. In each plot, the best elliptical aperture determined by sextractor for the ACS data is shown in green, the best aperture for the SHARDS image is plotted in red, and the circular aperture used to calibrate the SHARDS data is shown in black. The two panels in the last row show galaxies whose photometry (and probably the spectra) are affected by contamination from nearby sources. These sources were excluded from our calibration procedure. They are marked with gray symbols in Figure 5.

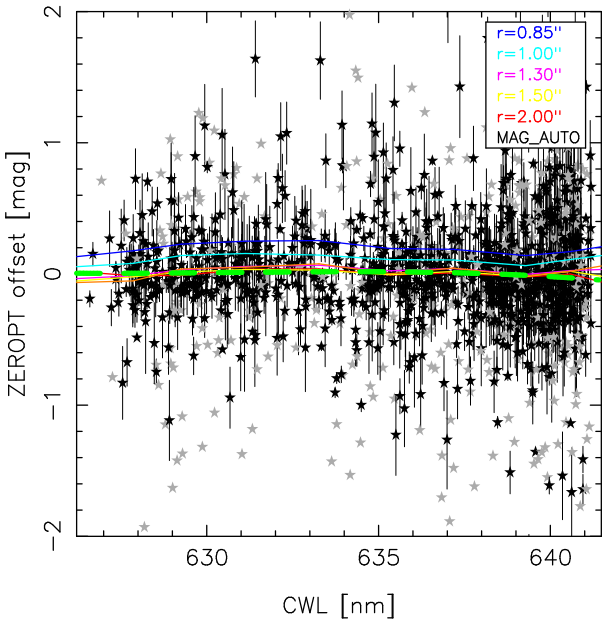

FIG. 5.— Calibration of the SHARDS data for filter F636W17 based on the HST/ACS spectra. The difference between the AB magnitude obtained from the spectra and the magnitude measured in the SHARDS images is plotted as a function of CWL of the pass-band seen by the galaxy (i.e., vs. position in the field-of-view, as described in Section 3.2.1 and defined by Equation 1). The points show the calibration obtained from individual galaxies for the best photometric aperture, i.e., the one enclosing the entire object and minimizing the uncertainties, the effects of seeing, and the contamination from close neighbors. Objects whose photometry is affected by nearby sources or have low-SNR spectra are plotted with gray symbols. Color continuous lines show the median behavior for the offset calculated with different aperture radii. The final calibration is shown with a black dashed line, resulting from a polynomial fit to the best aperture data.

age (see Table 1), typically 0.05–0.08 mag.

-Plot with synthetic data? Scatter from that plot at least

3.3. *Data quality*

The SHARDS data presented in this paper was obtained in queue mode, and a maximum seeing threshold was imposed in 0.9″. This image quality was imposed in order to reach the necessary flux limits to detect and reliably measure absorption indices for massive quiescent galaxies up to z∼2.5 (26.5-27.0 mag at the 3σ level). In Table 1, we show the final seeing of the SHARDS images, measured after carrying out all reduction and calibration steps. Virtually all SHARDS data was taken under sub-arcsec conditions.

Concerning the final depth of our images, we give in Table 1 the typical depths reached at the 3σ level, and the magnitude level corresponding to the third quartile of the brightness distribution. The desired depths were reached in most of the filters, with some presenting exceptional seeing and depth figures.

4. SHARDS SCIENCE VERIFICATION: EMISSION-LINE SYSTEMS

4.1. *ELGs at interm-z*

The study of star-forming galaxies and objects hosting AGN through the analysis of their emission-line spectra is one of the main tools in Astrophysics to understand galaxy evolution. Emission lines can be used to select this kind of galaxies, and then to obtain estimations of relevant physical parameters, being redshift, SFR, metallicity, or black hole mass some of the most interesting (e.g., Charlot & Longhetti 2001, []).

Although the most straight-forward way of getting emission-line identifications and fluxes is obtaining spectroscopic observations, these data are hard to obtain for large number of objects and very time consuming. Moreover, current spectrographs on the largest telescopes are only able to reach magnitudes around RI∼24-25. This translates to the fact that spectroscopic data are very scarce for faint objects, especially at z$\gtrsim$1.5, and that spectroscopic surveys are biased towards bright emission-line galaxies.

A powerful alternative to spectroscopic surveys are (ultra-)deep narrow-band imaging observations, which have been demonstrated to be useful to select emission-line galaxies (ELGs) at the faintest magnitude range, and measure important quantities such as equivalent widths and line fluxes (see, among many, Teplitz et al. 1998; Kodaira et al. 2003; Ouchi et al. 2004; Willis & Courbin 2005; Ly et al. 2007; Takahashi et al. 2007; Villar et al. 2008; Shioya et al. 2008; Nilsson et al. 2009; Guaita et al. 2010; Hayes et al. 2010a; Ly et al. 2011). In addition, although imaging data cannot directly provide with robust identifications and precise observed wavelengths for emission-lines, they certainly help in the determination of accurate photometric redshifts even for very high redshift sources based on the detection of both emission and absorption features.

Being SHARDS an ultra-deep medium-band survey, we have tested whether the data have a large enough spectral resolution to select ELGs and measure the relevant parameters (EW, flux). Imaging surveys in the optical aimed at selecting ELGs usually employ narrow-band filters, narrow meaning widths around 10 nm. SHARDS' filters are wider, the typical FWHM is 15 nm, but the depth, photometric accuracy, and imaging quality of the GTC data can cope with the lower spectral resolution (R∼50), compared to more classical narrow-band surveys.

Figure 7 shows an example of the selection of ELGs with SHARDS data for one of our 24 filters, the one centered at 687 nm (filter F687W17). The method is similar to that used by narrow-band surveys such as the ones rerefenced above: the flux in a given photometric band at wavelength $\lambda_{\rm line}$ is compared with the average flux around that wavelength. Sources with emission-lines lying inside the central filter would present an excess of flux compared to the average around it, these corresponding to the spectrum continuum.

Typical narrow-band surveys use a broad-band filter to determine the continuum (Villar et al. 2008; Takahashi et al. 2007; Sobral et al. 2009; Hayes et al. 2010b, e.g.,), or one or several narrow-band filters around a given one (Sobral et al. 2012; Lee et al. 2012). In our case, the contiguous spectral coverage of the optical window allows us to obtain a continuum determination by using the adjacent filters to a given one. This measurement is very robust, since it takes into account the intrinsic color of each galaxy in a close region around the spectral region of interest, rather than providing an average continuum value in a wide wavelength range, as would be the case for surveys using broad-band filters.

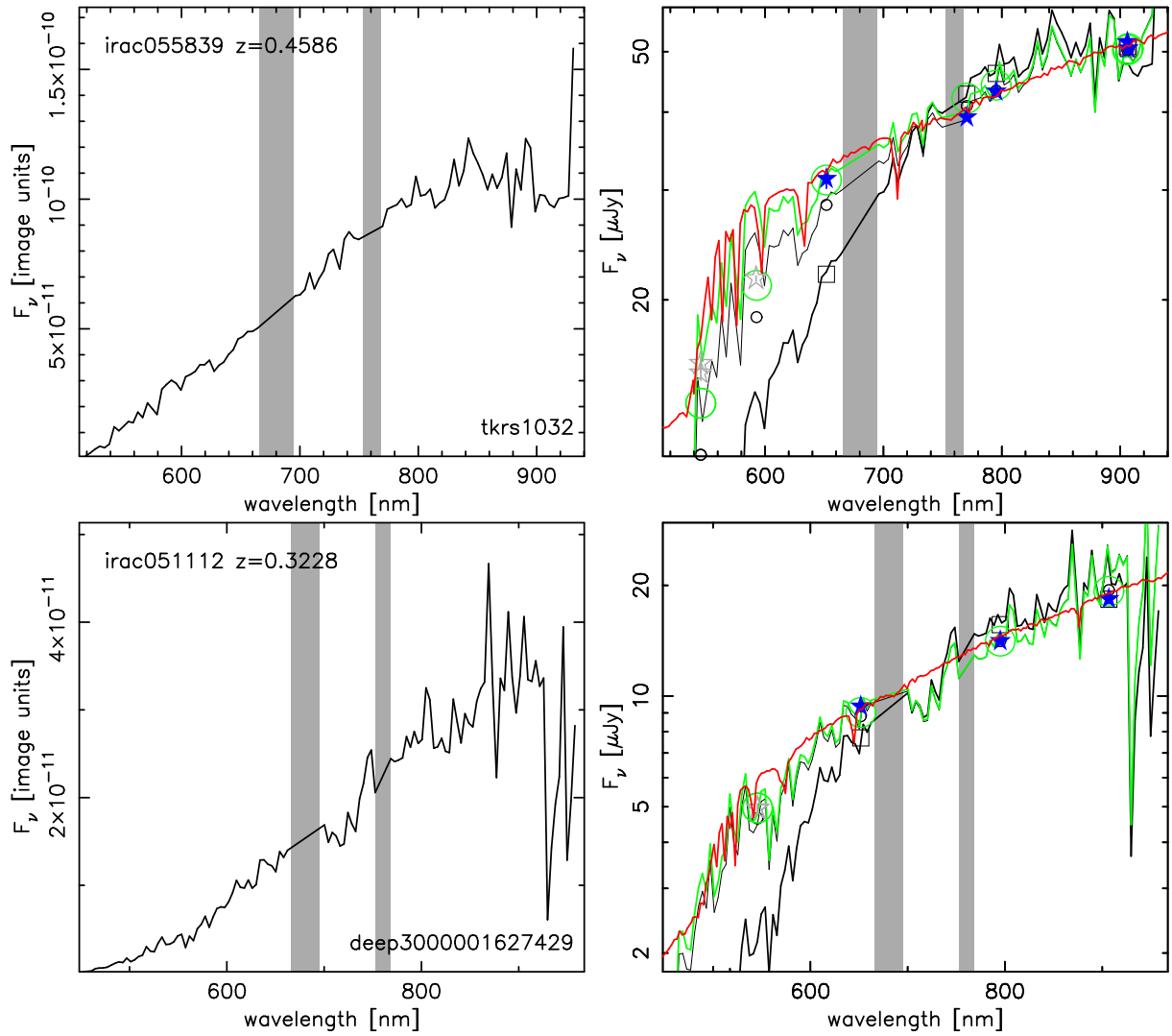

FIG. 6.— Two examples of the ground-based spectra used to test the absolute flux calibration of the SHARDS data. The original spectra are plotted on the left, indicating the name of the source in the Rainbow Cosmological Surveys database (Pérez-González et al. 2008) the TKRS and DEEP3 catalogs (Wirth et al. 2004; Cooper et al. 2011) and the spectroscopic redshift of each source. Both on the left and right panels we mark with a shaded area the regions where strong telluric absorption bands are located. On the right, we show in with a black thick line the original spectrum for each galaxy after flux scaling it with broad-band photometry, depicted with blue stars (for the reddest points, which provide a better absolute calibration) and gray symbols (for the bluest bands which are more affected by the spectral flat and atmospheric extinction corrections) stars. The black thin line shows the same spectrum after applying an average spectral flat obtained as explained in the text. The green line shows the final ground-based spectrum used for the calibration of SHARDS data, obtained after applying an atmospheric extinction correction calculated through a comparison with a stellar population synthesis model fitting the broad-band photometric data, shown in red in the plots. Black squares and circles, and green circles show the convolution of the previously described spectra (original after flux calibration, after spectral flat-fielding, and after extinction correction, respectively) with the transmission curves for the broad-band filters.

In order to understand the scatter in Figure 7, we have analyzed the photometric uncertainties for each galaxy. The distribution of the typical errors of our data is shown with a dashed line. Sources whose emission in the F687W17 filter is brighter than the average for the adjacent filters with more than the 3-σ confidence are located below the continuous orange line. This is the expected locus for emission-line galaxies. In this plot, we have marked with green symbols the galaxies with confirmed spectroscopic redshifts and for which the [OII] line would lie within the F687W17 pass-band[18]. We are able to recover more than 90% of the spectroscopically confirmed galaxies with an [OII] emission-line expected within the central filter. A visual inspection of the spectra for the non-selected objects revealed very weak or even absent [OII] emission-lines. Therefore, we conclude that the SHARDS data are very effective in isolating emission-line galaxies at a similar line flux level as deep spectroscopy.

It is also interesting to note that virtually all the spectroscopically confirmed ELGs in Figure 7 are brighter than $R{\sim}24.5$. This is the spectroscopic limit of the redshift surveys carried out in the GOODS-N field, and the typical detection threshold for the vast majority of data taken with state-of-the art spectrographs in 10-meter class telescopes. SHARDS observations reach at least 2 magnitudes fainter, opening the possibility to reliably

[18] Note that some of these galaxies may not present [OII] emission, being their spectroscopic redshifts based on some other spectral feature.

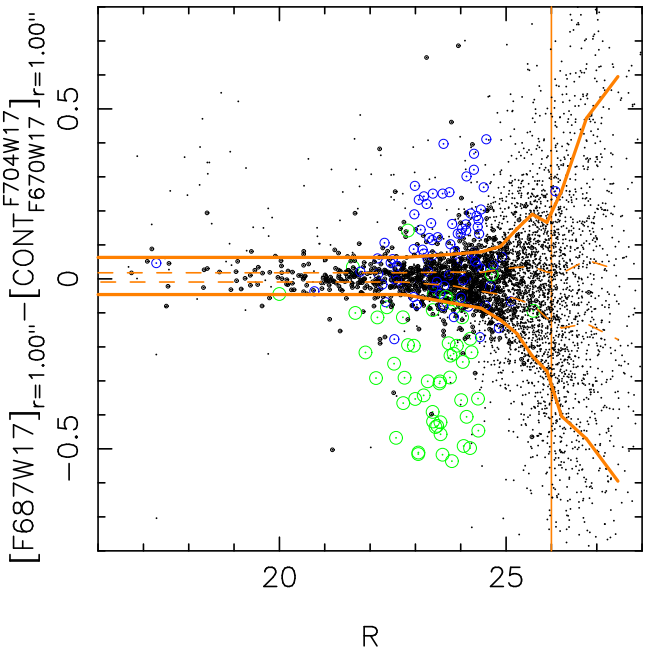

FIG. 7.— Color-magnitude diagram showing emission-line galaxy candidates at ∼687 nm in SHARDS pointing #1. The vertical axis shows the color between the F687W17 band and the average magnitude in the adjacent SHARDS bands (F670W17 and F704W17) measured within a circular aperture of radius r=1″. Sources with measured spectroscopic redshifts implying that the [OII] line lies within the F687W17 filter are marked in green, while sources whose [OII] emission is located in the adjacent filters are marked in blue. Solid points show galaxies with a photo-z between 0.7<z<0.9. The dashed orange lines depict the typical photometric uncertainty as a function of magnitude. ELGs with an emission line within the F687W17 filter detected with more than 3-σ confidence are found in the region below the bottom orange continuous line. ELGs with emission-lines within the F670W17 or F704W17 pass-bands should be located above the top orange continuous line. The vertical orange line shows the 5-σ detection threshold of the SHARDS survey in the F687W17 band. Only the sources detected by IRAC for which robust photometric redshifts were estimated (Pérez-González et al. 2008) are depicted.

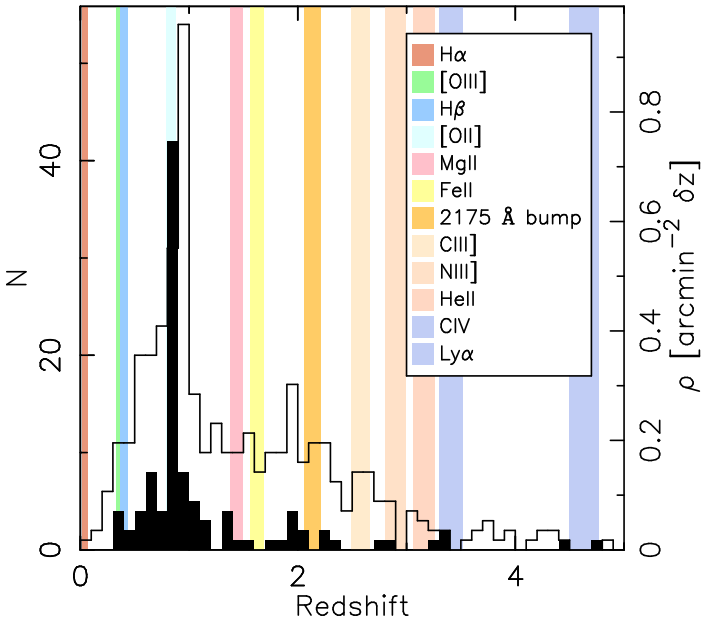

FIG. 8.— Photometric redshift distributions of the sources selected as ELGs with the F687W17 filter. The filled histogram shows the selected galaxies with spectroscopic redshifts. The open histogram shows all ELG candidates using photometric redshifts (Pérez-González et al. 2008). The expected redshifts for emitters with some of the most typical lines (e.g., Lyα, [OII], [OIII], or Hα) are marked with shadowed regions. We also mark spectral features such as the Mg-Fe absorption band at ∼280 nm, or the 2175 Å dust absorption bump (which would imprint an absorption in the galaxy SED).

select and study fainter and/or higher redshift ELGs.

Figure 8 shows the redshift distribution of the sources selected as ELGs by SHARDS with the F687W17 filter. The filled histogram represents galaxies with spectroscopic redshifts, i.e., confirmed ELGs. The open histogram shows the photometric redshifts (Pérez-González et al. 2008) for all ELG candidates. The redshift distributions show that the ELGs selected by SHARDS are preferentially located in the appropriate redshifts corresponding to the most common emission lines detected in intermediate and high redshift galaxies. The majority of the selected sample are [OII] emitters at z∼0.85, but significant redshift peaks are also observed where one expects other relevant lines such as [OIII], Hβ, AGN lines such as CIII] or CIV, and also Lyα.

Our observational strategy was conceived to detect and measure absorption bands. In this regard, the redshift distribution in Figure 8 also shows peaks around the regions where the Mg+Fe absorption band (at ∼280 nm) would move through the F687W17 passband (z∼1.5), around the Balmer or 4000 Å break (z=0.8–1.0), and also where the ISM dust absorption at 2175 Å peak could produce a differential attenuation from galaxy to galaxy. These absorption mimic an emission-line in a color-magnitude diagram such as the one depicted in Figure 7 (see also Figure 9).

Figure 9 shows eight examples of galaxies selected by SHARDS as emission-line sources and counting with spectroscopic confirmation. These sources have been selected using the F687W17 filter as central band. The two sources on the top row are example of low redshift (z∼0.3) galaxies detected because of their [OIII]$\lambda\lambda$4959,5007 emission. Comparing our photometry with the available spectroscopy for these galaxies, coming from Keck and HST/ACS grism data, we show that SHARDS is able to robustly identify emission lines and measure EWs and fluxes. Unlike the noisy spectra, our data allow to study the continuum (compare with the stellar population synthesis models shown in blue, which were fitted to the broad band data –see Pérez-González et al. 2008–). Using all the SHARDS photometric datapoints, we have estimated this continuum level and, combining this with the flux measurement for the F687W17 filter, we have obtained line fluxes and EWs. When comparing to the values obtained from the spectroscopy, we typically find smaller EWs. We interpret this systematic difference as an aperture effect, given that our photometric apertures are typically 1.0-1.5″ long in radius, probably larger than the typical slit widths and extraction sizes used in spectroscopic surveys. Note that larger apertures would easily dillute the emission lines in a brighter continuum, thus resulting in smaller measurements of the

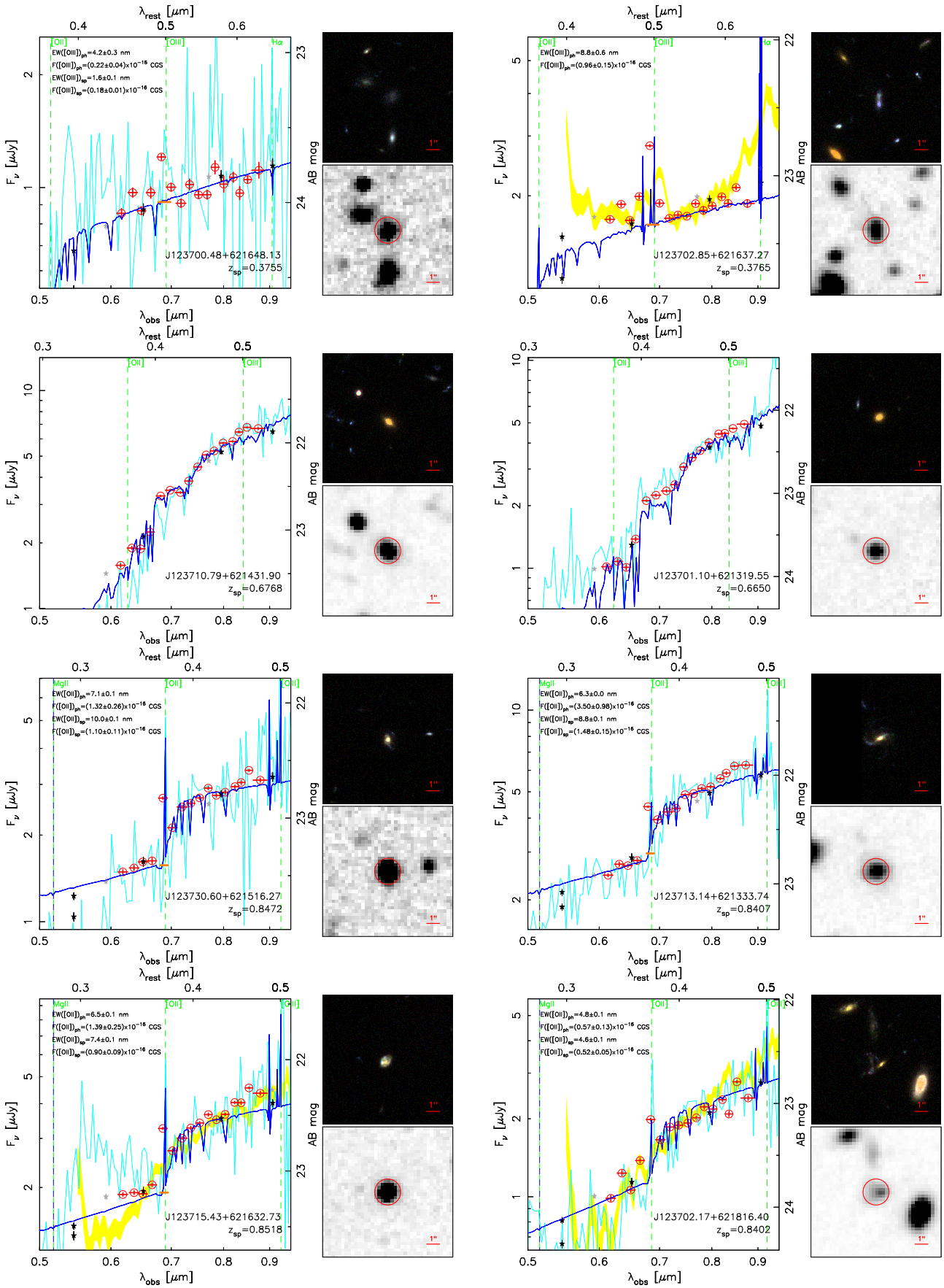

FIG. 9.— SEDs and postage stamps of some representative examples of the ELG candidates selected with the SHARDS F687W17 filter (from Figure 7). We show galaxies which have already been spectroscopically confirmed. On the left panel for each galaxy, we depict the optical SED of the source. Broad-band photometric fluxes are depicted with black (ground-based) and gray (HST) filled stars. Red symbols show the SHARDS data. Blue lines represent stellar population synthesis models fitting the broad-band data, which were used to obtain an estimation of the photometric redshift and stellar mass Pérez-González et al. (2008). The cyan lines show the ground-based spectrum (when available), after the spectral and absolute flux calibration explained in Section 3.1. For some sources, we also depict with a yellow shaded area the available HST/ACS grism spectrum from PEARS (including uncertainties). The wavelength for several typical emission-lines are marked in green. We also give measurements of EWs and fluxes for the [OII] and [OII] lines when it lies within the F687W17 filter pass-band, using both the spectroscopic and the photometric SHARDS data. On the right for each galaxy, we show postage stamps in the ACS bands (RGB image) and the SHARDS F687W17 filter. North is up and East is left; image sizes are $10'' \times 10''$.

EW. Flux measusrement must be more robust, and indeed our estimations of the line fluxes are in very good agreement with the spectrocopic measurements (when available).

On the second row of Figure 9, we show two examples of galaxies located in the ELG locus in Figure 9, but not showing emission lines. These sources were selected due to the significant flux difference between adjacent bands around the 687 nm filter. In this case, this large color is due to the presence of the Balmer or 4000 Å break at approximately 680 nm (compare with the spectra and stellar population synthesis models). These Balmer break/D(4000) sources from the redshift tail between the z∼0.84 peak, which corresponds to [OII] emitters, and z∼1.2 seen in the redshift histogram in Figure 8. The postage stamps show that these sources are typically red spheroids, where strong 4000 Å breaks are expected. Again, our SHARDS data is able to probe this spectral region with high accuracy and measure absorption indices such as the D(4000). We refer the reader to Section 5 for a discussion of the detection of absorption features with SHARDS data and the effect on the uncertainties of the parameters derived with stellar population synthesis models.

The third and fourth rows in Figure 9 show [OII] emitters with spectroscopic confirmation (from Keck and HST grism data) selected in the F687W17 band ([OII] around z=0.84). These are typical examples where it is clearly demonstrated that SHARDS data is able to detect faint emission-line galaxies, which may be even missed by low resolution spectroscopy such as that from HST/ACS grism data. This is the case for the sources in the bottom row, whose [OII] emission is not measurable with HST/ACS data, but confirmed with ground-based medium-resolution spectroscopy. We would also like to notice that our medium-band spectro-photometric data are able to detect and robustly measure emission-lines as faint as $\sim 5\times10^{-17}$ erg s^{-1} cm^{-2}.

In summary, our science verification test has demonstrated that SHARDS is able to detect virtually all the spectroscopically confirmed emission-line galaxies at intermediate redshift, opening the possibility to extend and reach higher completeness in the samples of ELGs in GOODS-N, and carry out a comprehensive analysis of star-forming galaxies and AGN down to fainter magnitudes (∼26.5 mag) than spectroscopic surveys. A complete analysis of the properties of the emission-line galaxies detected by SHARDS will be presented in a forthcoming paper (Cava et al. 2012, in preparation).

More comments on galaxies

Victor comments, including references

4.2. *ELGs at very high-z*

The ultra-deep imaging data from SHARDS could, in principle, allow to detect and study sources at very high-z (z$\gtrsim$3). Indeed, reaching magnitudes as faint as 26.5-27.0 mag in all bands from 500 to 941 nm is deep enough to detect interesting sources such as Lyα emitters (LAEs) at z> 3 and up tp z∼6.7 (REFs). Figure 9 showed examples of ELGs at intermediate redshift (z$\lesssim$1). In Figure 10, we show one example of a spectroscopically confirmed AGN at z>3 where SHARDS data reveals the presence of several emission lines such as CIII]λ1909 or CIVλ1548. The SED of this AGN shows that the spectro-photometric data from SHARDS is completely consistent and provides a similar spectral resolution as the HST grism data from PEARS. Our data provide very robust fluxes and flux densities for both emission-lines and the continuum for a source which is as faint as the typical spectroscopic limit of ground-based state-of-the-art spectrographs in 10m class telescopes (see the noisy Keck spectrum for this source).

A preliminary analysis of the SHARDS data in four filters revealed a dozen dropout sources with SEDs consistent with z>4 LAEs and LBGs. Figure 10 shows one of these LAE candidates at z∼5. We refer the reader to Rodriguez-Espinosa et al. (2012ab) for a more detailed discussion on the detection and properties of the LAEs detected by SHARDS.

5. SHARDS SCIENCE VERIFICATION: ABSORPTION SYSTEMS

The main goal of the SHARDS project is analyzing in detail the stellar populations in the massive red galaxies at high redshift which are already evolving passively. The survey observational strategy is aimed at constructing rest-frame UV/optical SEDs for this kind of sources with enough spectral resolution to be able to measure absorption indices correlated with important physical parameters such as the age of the stellar populations.

The main absorption index targeted by SHARDS for high-z red and dead sources is the Mg index, Mg$_{UV}$. This index probes several absorption lines (e.g., MgIλ2852, MgIIλ2800, FeIλ??) and has been shown to be a extremely reliable means to detect quiescent massive galaxies. Indeed, the rest-frame UV spectra of red and dead galaxies is very red and the presence of the absorption lines can be used to easily distinguish their SED from the featureless spectrum of a dusty starburst (Daddi et al. 2005a). The relative intensity of these absorptions can be measured with the Mg$_{UV}$ spectral index, directly linked to the age of the stellar population (e.g., Bruzual & Charlot 1993). The index is easily and robustly measurable in low resolution spectra (R<100, Daddi et al. 2005a). The index has been successfully used in the past to obtain redshifts and ages of stellar populations in massive galaxies at high-z (Spinrad et al. 1997; Cimatti et al. 2004; McCarthy et al. 2004; Saracco et al. 2005; Daddi et al. 2005a).

Other interesting absorption features which are probed by SHARDS are the Balmer and 4000 Å break, or the Ca HK lines, the G-band, or the Mg$_1$, Mg$_2$ and TiO$_2$ molecular bands (among others). All these have been extensively used to study stellar population ages (among many, Burstein et al. 1984; Worthey 1994; Worthey et al. 1994; Balogh et al. 1999; Franx et al. 2003; Kauffmann et al. 2003b; Förster Schreiber et al. 2004; Gallazzi et al. 2005; Kriek et al. 2006, 2011; Muzzin et al. 2012, see also the review by Renzini 2006). The spectral resolution of the SHARDS dataset is adequate for measuring the Balmer or (D4000) breaks with the same accuracy as the one achieved in spectroscopic studies of nearby galaxies and synthesis models, which typically use bands of 10–20 nm around the feature (Bruzual A. 1983). In the case of the molecular bands, the SHARDS' filter widths are larger than the amplitude of these absorptions, but, given their strength, they should affect the photometry in filters such as ours. In addition, as demonstrated in

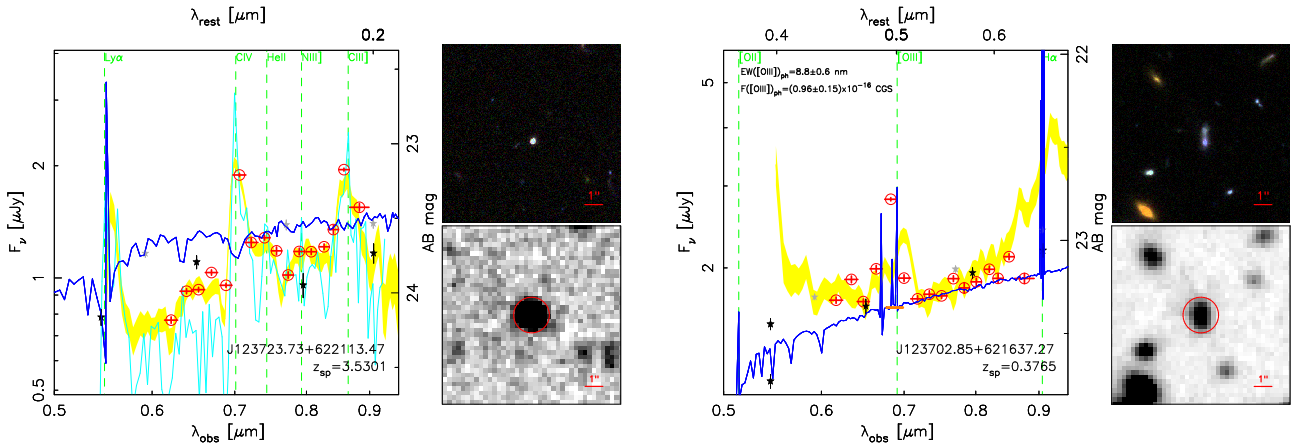

FIG. 10.— Examples of SEDs constructed with SHARDS data for z>3 galaxies. Symbols and lines are the same as the ones explained in Figure 9. On the left, we show an AGN at z∼3.5 with clear detections of emission-lines such as CIII and CIV with the SHARDS spectro-photometric data. On the right, we show a dropout source which has been selected as a candidate for a LAE at z∼5 (Rodriguez-Espinosa et al. 2012ab). STILL NEEDS A LAE FOR THE SECOND EXAMPLE!!

the previous Section, SHARDS data is also very sensitive to emission lines, so they can be used to detect low level residual (unobscured) star formation in massive galaxies at high-z and confirm their quiescent (jointly with other methods, such as the study of the MIR/FIR emission).

In this Section, in order to demonstrate the power of the SHARDS dataset to accurately measure absorption indices, we present the SEDs built with SHARDS data for spectroscopically confirmed red and dead massive galaxies at z>1. Rather than measuring and studying one specific absorption index, we fit the entire SED of each galaxy, also including broad-band data up to the MIR wavelengths probed by *Spitzer*/IRAC data. We, therefore, use all the information available for our sample of red and dead massive galaxies to carry out the most reliable analysis of their stellar population properties. We concentrate our study on z>1 to be sure that the D(4000) and/or Mg_{UV} absorption features are probed by the available data so far.

The sample compiled for this science demonstration exercise has been extracted from several sources in the literature. We include the three galaxies (classified as *red nuggets*) whose dynamical masses were studied in (Newman et al. 2010) and are covered by our data. We also include four galaxies at z>1 from (Ferreras et al. 2009), who concentrated in intermediate redshift galaxies but had a few z>1 galaxies in their sample. Given that the galaxies in this paper count with pseudo-spectrocopic redshifts coming from HST optical grism data, we compared the quoted redshifts with our photometric redshifts and only selected the four galaxies with consistent estimations. Finally, we also selected galaxies qualifying as Extremely Red Objects (ERO) following the definition in Elston et al. (1988) and citet2000AJ....120..575Y and/or Distant Red Galaxies at z>1 (Franx et al. 2003), according to their observed optical and NIR colors. In order to avoid dusty starburst in this study and concentrate in massive galaxies with evolved stellar populations, we only considered the galaxies undetected in the 24 μm data, which reach fluxes as low as 30 μJy in GOODS-N (reduction and catalogs described in Pérez-González et al. 2005 and Pérez-González et al. 2008). The final sample considered in the following discussion is composed by 27 galaxies whose main properties are given in Table 2.

The SEDs for the sample of 27 massive red and dead galaxies at z>1 were fitted with several of the most common stellar population libraries found in the literature. We considered general exponential decaying models using the predictions from the following codes:

- the PEGASE code (Fioc & Rocca-Volmerange 1997, P01), assuming a Kroupa (2001) initial mass function (IMF).
- the (Bruzual & Charlot 2003) models (BC03) with a (Chabrier 2003) IMF.
- the Charlot & Bruzual 2009 models (CB09) with a Kroupa or Chabrier IMFs.
- and the Maraston (2005) models (M05) with a Kroupa IMF.

In all cases, we considered the following mass limits for the IMF: $0.1<\mathcal{M}<100\ \mathcal{M}_{\odot}$.

The fitting procedure is explained in detail in Pérez-González et al. (2003) and Pérez-González et al. (2008). Briefly, the photometry is compared with the models assuming and exponentially decreasing SFH characterized by a τ parameter which runs from 1 Myr (almost identical to a single stellar population) to 12 Gyr (almost constant SFH). We run models corresponding to the different metallicities given for each library, which run from $Z_{\odot}/200$ to $2.5\times Z_{\odot}$ for BC03 and CB09 models, $Z_{\odot}/200$ to $5\times Z_{\odot}$ for P01, and $Z_{\odot}/50$ to $2\times Z_{\odot}$ for M05 models. We considered an extinction parametrized with a A(V) value running from 0 mag to 2 mag, with the extinction law following the law published in (Calzetti et al. 2000). Finally, all ages between 1 Myr to 15 Gyr were probed to search for the best fitting model minimizing a χ^2 maximum-likelihood estimator.

In order to study the uncertainties in the derived parameters and take into account the possible degeneracies in the solutions, we run Montecarlo simulations for each galaxy, randomly varying the photometric datapoints with a Gaussian distribution of width equal to the photometric uncertainty, and repeating the fit again to all possible models. We run the code 1000 times and then

analyzed the solutions. This analysis consisted on identification of clusters of solutions with a k-means method. Typically, 1 to 3 clusters of solutions were identified for each galaxy. These different solutions provided with information about the typical degeneracies of the study of stellar populations, such as the age-metallicity degeneracy or the one linked to τ-value and age. For each cluster, we assigned a probability value given by the number of solutions belonging to the solutions. In all cases, one solution was dominant, with more than 50% of the solution data points belonging to it. Table 2 shows the different solutions for each galaxy and the statistical weight of each of them.

In Figure 11, we show several representative examples of the stellar populations synthesis SED modeling and results for massive quiescent galaxies with a spectroscopic redshift above z=1. For each galaxy in this figure, we depict the complete SED and best fitting models for the different libraries mentioned above, jointly with a close-up look into the rest-frame UV/optical range probed by the SHARDS data, several plots showing the results of the synthesis models, and postage stamps in HST and SHARDS filters.

The galaxy shown at the top of Figure 11 lies at z$\sim$1.25 and our currently available SHARDS data do not cover the Mg_{UV} absorption feature. The stellar population synthesis analysis shows that there are at least 4 different clusters of solutions. Two clusters are consistent with SSPs (one with solar metallicity, the other one with subsolar abundances) with ages between 1 and 5 Gyr, and another 2 with τ values between 100 Myr and 1 Gyr. The latter are significantly more statistically representative than the former (i.e., models do not favot SSPs). All solutions are consistent with an extinction around A(V)=0.3 mag and we find stellar masses within a 0.3dex around $10^{10.8-11.2}$ $M_\odot$. Interestingly, different models predict significantly different values for the relevant parameters, especially for the age and τ values.

The second example in Figure 11 shows a z=1.29 where we have been able to measure the Mg_{UV} index, apart from other spectral features such as ??. The stellar population synthesis degeneracies are considerably smaller than in the first example. Indeed, there is a dominant solution corresponding to a star-forming burst with $\tau$$\sim$100 Myr, age around 1 Gyr, A(V)=0.3 mag, solar metallicity and mass $10^{10.3}$ $M_\odot$. Although this solution clearly dominates for the fidual model, CB09-chab, other libraries achieve different results, although with very similar statistical weight (i.e., one solution dominates for all different models).

Finally, the last example in Figure 11 shows the source at the highest redshift in our sample. Similarly to the previous source, one solution clearly dominates, with parameters $\tau$$\sim$100 Myr, age around 0.6 Gyr, A(V)=0.3 mag, solar metallicity and mass $10^{10.3}$ $M_\odot$. Our fiducial model, however, seems to provide a different solution to all the restof models, which favor a slightly more extended SFH, older population (2 Gyr) and heavier masses ($10^{10.7}$ $M_\odot$).

In order to test how the spectro-photometric data from SHARDS helps in the stellar population synthesis modelling of the massive quiescent galaxies at z>1, we compare in Figure **??** the results obtained when fitting only the broad-band data for the galaxy at z=1.40 with those obtained when adding the SHARDS data.

Absorption vs. extinction

ages, bursty?, star formation mode, chi2 discussion

AGN with 2175 AA bump?

BzK diagram of sources in this section compared to all SHARDS sources

Fig: Comparison with broad-band results

Fig: SFH of massive galaxies

Fig?: Comparison between models

Completeness of sample compared to EROs

5.1. *Improvements in modeling*

2175 AA bump.

6. SUMMARY

ACKNOWLEDGMENTS

We acknowledge support from the Spanish Programa Nacional de Astronomía y Astrofísica under grants AYA2009-07723-E and AYA2009-10368. SHARDS has been funded by the Spanish MICINN under the Consolider-Ingenio 2010 Program grant CSD2006-00070: First Science with the GTC. This work has made use of the Rainbow Cosmological Surveys Database, which is operated by the Universidad Complutense de Madrid (UCM). We thank all the GTC Staff for their support and enthusiasm with the SHARDS project, and we would like to especially acknowledge the help from Antonio Cabrera and René Rutten. IRAF!!, GTC, CAHA

REFERENCES

Abramo, L. R. et al. 2011, ArXiv e-prints
Arnouts, S. et al. 2007, A&A, 476, 137
Balogh, M. L., Morris, S. L., Yee, H. K. C., Carlberg, R. G., & Ellingson, E. 1999, ApJ, 527, 54
Barger, A. J., Cowie, L. L., & Wang, W.-H. 2008, ApJ, 689, 687
Barro, G. et al. 2011a, ApJS, 193, 13
—. 2011b, ApJS, 193, 30
Bauer, A. E., Drory, N., Hill, G. J., & Feulner, G. 2005, ApJ, 621, L89
Baugh, C. M., Cole, S., Frenk, C. S., & Lacey, C. G. 1998, ApJ, 498, 504
Bell, E. F., Phleps, S., Somerville, R. S., Wolf, C., Borch, A., & Meisenheimer, K. 2006, ApJ, 652, 270
Bell, E. F. et al. 2004, ApJ, 608, 752
Benítez, N. et al. 2009a, ApJ, 691, 241
—. 2009b, ApJ, 692, L5
Borch, A. et al. 2006, A&A, 453, 869
Bruzual, A., & Charlot, S. 1993, ApJ, 405, 538
Bruzual, G., & Charlot, S. 2003, MNRAS, 344, 1000
Bruzual A., G. 1983, ApJ, 273, 105
Burstein, D., Faber, S. M., Gaskell, C. M., & Krumm, N. 1984, ApJ, 287, 586
Calzetti, D., Armus, L., Bohlin, R. C., Kinney, A. L., Koornneef, J., & Storchi-Bergmann, T. 2000, ApJ, 533, 682
Caputi, K. I. et al. 2006, ApJ, 637, 727
Cardamone, C. N. et al. 2010, ApJS, 189, 270
Cepa, J. 2010, in Highlights of Spanish Astrophysics V, ed. J. M. Diego, L. J. Goicoechea, J. I. González-Serrano, & J. Gorgas, 15
Cepa, J. et al. 2011, in Highlights of Spanish Astrophysics VI, ed. M. R. Zapatero Osorio, J. Gorgas, J. Maíz Apellániz, J. R. Pardo, & A. Gil de Paz, 167–172
Chabrier, G. 2003, ApJ, 586, L133
Charlot, S., & Longhetti, M. 2001, MNRAS, 323, 887
Cimatti, A. et al. 2008, A&A, 482, 21
—. 2004, Nature, 430, 184

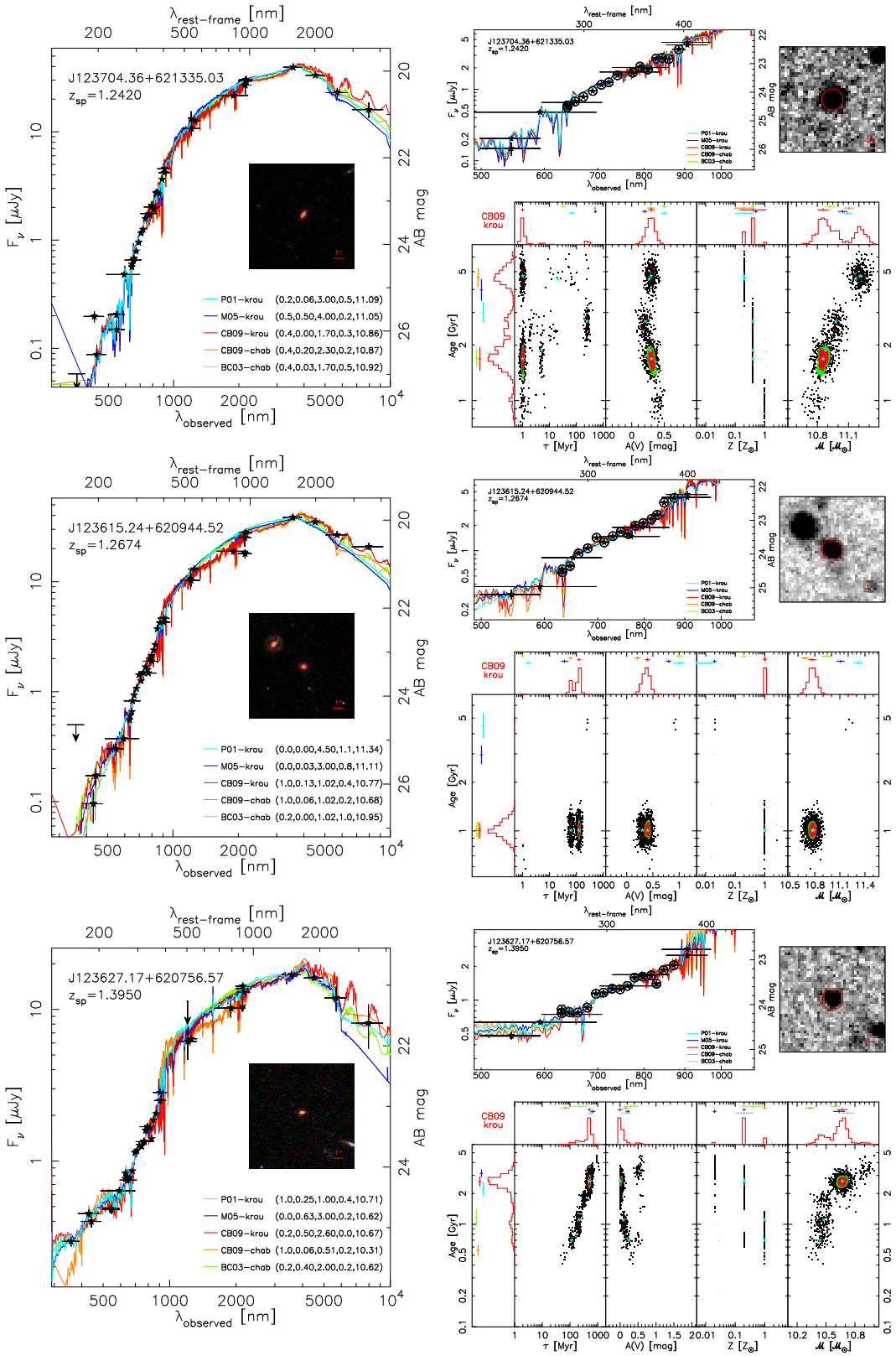
J123704.36+621335.03
z_sp=1.2420
P01−krou (0.2,0.06,3.00,0.5,11.09)
M05−krou (0.5,0.50,4.00,0.2,11.05)
CB09−krou (0.4,0.00,1.70,0.3,10.86)
CB09−chab (0.4,0.20,2.30,0.2,10.87)
BC03−chab (0.4,0.03,1.70,0.5,10.92)
J123615.24+620944.52
z_sp=1.2674
P01−krou (0.0,0.00,4.50,1.1,11.34)
M05−krou (0.0,0.03,3.00,0.8,11.11)
CB09−krou (1.0,0.13,1.02,0.4,10.77)
CB09−chab (1.0,0.06,1.02,0.2,10.68)
BC03−chab (0.2,0.00,1.02,1.0,10.95)
J123627.17+620756.57
z_sp=1.3950
P01−krou (1.0,0.25,1.00,0.4,10.71)
M05−krou (0.0,0.63,3.00,0.2,10.62)
CB09−krou (0.2,0.50,2.60,0.0,10.67)
CB09−chab (1.0,0.06,0.51,0.2,10.31)
BC03−chab (0.2,0.40,2.00,0.2,10.62)
CB09 krou
λrest−frame [nm]
λobserved [nm]
Fν [μJy]
AB mag
Age [Gyr]
τ [Myr]
A(V) [mag]
Z [Z⊙]
M [M⊙]

FIG. 11.—

TABLE 2
STELLAR POPULATION SYNTHESIS RESULTS FOR RED AND DEAD GALAXIES AT z>1.

Galaxy (1)	z (2)	Model (3)	τ (4)	Age (5)	A(V) (6)	Z (7)	M (8)	χ^2 (9)	Prob. (10)
J123704.36+621335.03	1.2420	BC03-chab	32^{+8}_{-7}	$1.71^{+0.18}_{-0.18}$	$0.50^{+0.05}_{-0.05}$	$0.40^{0.00}_{0.00}$	$10.9204^{+0.0419}_{-0.0474}$	$0.7^{+1.0}_{-0.4}$	96.0
		CB09-chab	496^{+47}_{-50}	$4.75^{+0.52}_{-0.49}$	$0.30^{+0.04}_{-0.04}$	$0.20^{0.22}_{0.00}$	$11.0997^{+0.0461}_{-0.0374}$	$0.8^{+1.1}_{-0.5}$	35.6
		CB09-krou	$1.0^{+0.1}_{-0.1}$	$1.69^{+0.23}_{-0.21}$	$0.30^{+0.04}_{-0.05}$	$0.40^{0.68}_{0.00}$	$10.8638^{+0.0440}_{-0.0481}$	$0.9^{+1.2}_{-0.6}$	49.7
		M05-krou	501^{+50}_{-53}	$4.02^{+0.48}_{-0.36}$	$0.20^{+0.05}_{-0.04}$	$0.50^{0.00}_{0.00}$	$11.0464^{+0.0428}_{-0.0377}$	$0.7^{+0.9}_{-0.5}$	56.5
		P01-krou	69^{+20}_{-14}	$3.00^{+0.37}_{-0.33}$	$0.50^{+0.04}_{-0.05}$	$0.20^{0.20}_{0.00}$	$11.0874^{+0.0468}_{-0.0537}$	$0.8^{+1.1}_{-0.5}$	87.6
J123615.24+620944.52	1.2674	BC03-chab	$1.0^{+0.1}_{-0.1}$	$1.02^{+0.13}_{-0.11}$	$1.00^{+0.04}_{-0.05}$	$0.20^{0.00}_{0.00}$	$10.9443^{+0.0452}_{-0.0420}$	$0.7^{+1.0}_{-0.5}$	88.9
		CB09-chab	$1.0^{+0.1}_{-0.1}$	$0.72^{+0.09}_{-0.08}$	$0.40^{+0.05}_{-0.04}$	$1.00^{0.00}_{0.00}$	$10.6605^{+0.0470}_{-0.0422}$	$0.9^{+1.2}_{-0.6}$	34.8
		CB09-krou	116^{+17}_{-47}	$1.02^{+0.10}_{-0.10}$	$0.37^{+0.05}_{-0.06}$	$1.00^{0.00}_{0.98}$	$10.7748^{+0.0423}_{-0.0456}$	$0.8^{+1.2}_{-0.5}$	99.6
		M05-krou	36^{+11}_{-10}	$3.01^{+0.46}_{-0.31}$	$0.80^{+0.05}_{-0.05}$	$0.02^{0.00}_{0.00}$	$11.1140^{+0.0464}_{-0.0436}$	$0.8^{+1.1}_{-0.5}$	70.5
		P01-krou	$1.6^{+0.4}_{-0.5}$	$4.48^{+0.55}_{-0.60}$	$1.01^{+0.10}_{-0.10}$	$0.00^{0.01}_{0.00}$	$11.3185^{+0.0494}_{-0.0459}$	$0.8^{+1.1}_{-0.5}$	78.1
J123627.17+620756.57	1.3950	BC03-chab	218^{+38}_{-29}	$1.12^{+0.25}_{-0.17}$	$0.33^{+0.17}_{-0.06}$	$0.40^{0.60}_{0.21}$	$10.5910^{+0.0431}_{-0.0545}$	$1.6^{+2.2}_{-1.2}$	59.9
		CB09-chab	69^{+30}_{-8}	$0.56^{+0.08}_{-0.08}$	$0.16^{+0.06}_{-0.12}$	$1.00^{0.00}_{0.64}$	$10.3246^{+0.0416}_{-0.0463}$	$2.2^{+2.9}_{-1.7}$	81.1
		CB09-krou	501^{+59}_{-55}	$2.60^{+0.31}_{-0.24}$	$0.01^{+0.05}_{-0.01}$	$0.20^{0.00}_{0.18}$	$10.6719^{+0.0595}_{-0.0448}$	$2.2^{+2.9}_{-1.6}$	75.0
		M05-krou	160^{+24}_{-21}	$1.51^{+0.18}_{-0.17}$	$0.00^{+0.06}_{-0.00}$	$0.02^{3.03}_{0.00}$	$10.4077^{+0.0480}_{-0.0471}$	$2.2^{+2.8}_{-1.7}$	35.4
		P01-krou	572^{+121}_{-100}	$2.25^{+0.38}_{-0.36}$	$0.18^{+0.13}_{-0.09}$	$0.20^{0.20}_{0.18}$	$10.7227^{+0.0693}_{-0.0528}$	$1.9^{+2.6}_{-1.4}$	58.0
J123738.71+621727.86	1.2907	BC03-chab	56^{+9}_{-9}	$2.61^{+0.35}_{-0.25}$	$0.20^{+0.05}_{-0.05}$	$0.20^{0.00}_{0.00}$	$11.1788^{+0.0478}_{-0.0464}$	$1.0^{+1.3}_{-0.6}$	91.9
		CB09-chab	63^{+7}_{-7}	$1.02^{+0.11}_{-0.11}$	$0.00^{+0.05}_{-0.00}$	$1.00^{0.00}_{0.00}$	$10.8272^{+0.0512}_{-0.0500}$	$1.2^{+1.7}_{-0.8}$	100.0
		CB09-krou	135^{+23}_{-16}	$2.58^{+0.29}_{-0.22}$	$0.10^{+0.04}_{-0.05}$	$0.20^{0.00}_{0.00}$	$11.1466^{+0.0478}_{-0.0424}$	$1.2^{+1.6}_{-0.8}$	36.6
		M05-krou	$1.0^{+0.1}_{-0.1}$	$4.02^{+0.45}_{-0.38}$	$0.50^{+0.05}_{-0.04}$	$0.02^{0.00}_{0.00}$	$11.3156^{+0.0429}_{-0.0440}$	$1.1^{+1.5}_{-0.7}$	100.0
		P01-krou	484^{+61}_{-95}	$3.38^{+0.41}_{-0.31}$	$0.21^{+0.04}_{-0.05}$	$0.20^{0.00}_{0.18}$	$11.2311^{+0.0447}_{-0.0409}$	$1.1^{+1.6}_{-0.8}$	88.5
J123553.07+621044.47	1.4000	BC03-chab	624^{+65}_{-80}	$2.28^{+0.27}_{-0.24}$	$1.10^{+0.05}_{-0.06}$	$0.20^{0.20}_{0.00}$	$10.8091^{+0.0465}_{-0.0477}$	$0.6^{+0.9}_{-0.4}$	89.1
		CB09-chab	211^{+19}_{-27}	$1.08^{+0.10}_{-0.14}$	$0.69^{+0.08}_{-0.05}$	$1.00^{0.00}_{0.60}$	$10.5237^{+0.0391}_{-0.0595}$	$0.8^{+1.2}_{-0.6}$	44.4
		CB09-krou	471^{+70}_{-59}	$2.04^{+0.30}_{-0.33}$	$0.86^{+0.07}_{-0.24}$	$0.20^{0.20}_{0.00}$	$10.7022^{+0.0504}_{-0.0516}$	$0.8^{+1.2}_{-0.6}$	66.9
		M05-krou	1222^{+168}_{-169}	$3.93^{+0.43}_{-0.41}$	$1.09^{+0.05}_{-0.06}$	$0.02^{0.50}_{0.00}$	$10.8342^{+0.0545}_{-0.0488}$	$0.8^{+1.1}_{-0.5}$	70.5
		P01-krou	1651^{+377}_{-348}	$3.66^{+0.61}_{-0.54}$	$1.09^{+0.06}_{-0.09}$	$0.20^{0.20}_{0.18}$	$10.9287^{+0.0517}_{-0.0444}$	$0.8^{+1.1}_{-0.5}$	91.8

NOTE. — (1) Name of the galaxy (including J2000 coordinates). (2) Spectroscopic redshift from the literature (see text for references). (4) Exponential decay factor and uncertainty of the best fitting model (in Myr). (5) Age and uncertainty (in Gyr) of the best fitting model. (6) Extinction in the V-band and uncertainty (in mag) of the best fitting model. (7) Metallicity and uncertainty (solar units) of the best fitting model. (8) Stellar mass and uncertainty (solar units). (9) Median and 68% range for the goodness of the fit (χ^2 value). (10) Statistical significance of this solution (in %).

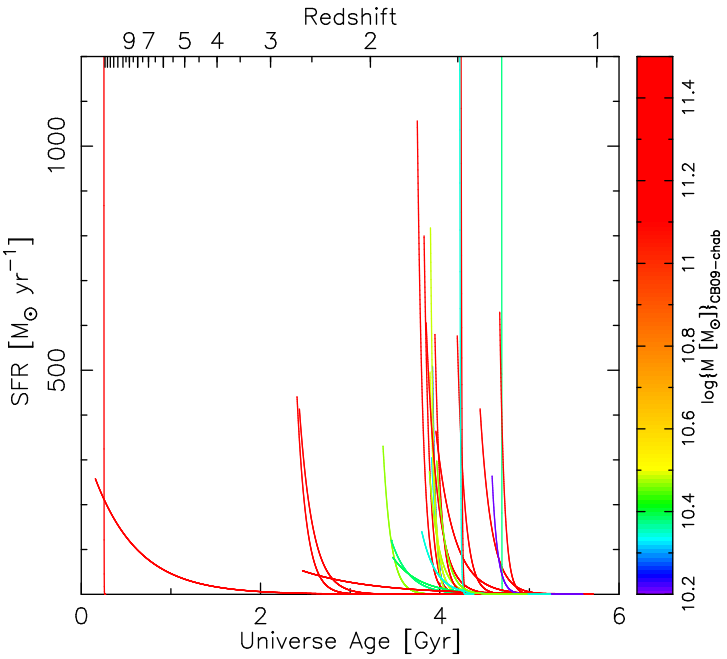

FIG. 12.—

Cole, S., Lacey, C. G., Baugh, C. M., & Frenk, C. S. 2000, MNRAS, 319, 168
Colless, M. et al. 2001, MNRAS, 328, 1039
Conselice, C. J., Bershady, M. A., Dickinson, M., & Papovich, C. 2003, AJ, 126, 1183
Cooper, M. C. et al. 2011, ApJS, 193, 14
Cowie, L. L., Barger, A. J., Hu, E. M., Capak, P., & Songaila, A. 2004, AJ, 127, 3137
Cowie, L. L., Songaila, A., Hu, E. M., & Cohen, J. G. 1996, AJ, 112, 839
Croton, D. J. et al. 2006, MNRAS, 365, 11
Daddi, E., Cimatti, A., Renzini, A., Fontana, A., Mignoli, M., Pozzetti, L., Tozzi, P., & Zamorani, G. 2004, ApJ, 617, 746
Daddi, E. et al. 2005a, ApJ, 631, L13
—. 2005b, ApJ, 626, 680
De Lucia, G., & Blaizot, J. 2007, MNRAS, 375, 2
Eggen, O. J., Lynden-Bell, D., & Sandage, A. R. 1962, ApJ, 136, 748
Eisenstein, D. J. et al. 2005, ApJ, 633, 560
Elbaz, D. et al. 2011, A&A, 533, A119
Ellis, R., Santos, M. R., Kneib, J.-P., & Kuijken, K. 2001, ApJ, 560, L119
Ellis, R. S., Abraham, R. G., Brinchmann, J., & Menanteau, F. 2000, Astronomy and Geophysics, 41, 020000
Elsner, F., Feulner, G., & Hopp, U. 2008, A&A, 477, 503
Elston, R., Rieke, G. H., & Rieke, M. J. 1988, ApJ, 331, L77
Faber, S. M. et al. 1997, AJ, 114, 1771
—. 2007, ApJ, 665, 265
Ferreras, I. et al. 2009, ApJ, 706, 158
Fioc, M., & Rocca-Volmerange, B. 1997, A&A, 326, 950
Fontana, A. et al. 2006, A&A, 459, 745
Förster Schreiber, N. M. et al. 2004, ApJ, 616, 40
Franx, M. et al. 2003, ApJ, 587, L79
Frayer, D. T. et al. 2006, ApJ, 647, L9
Gallazzi, A., Charlot, S., Brinchmann, J., White, S. D. M., & Tremonti, C. A. 2005, MNRAS, 362, 41
Gaztañaga, E., Cabré, A., & Hui, L. 2009, MNRAS, 399, 1663
Glazebrook, K. et al. 2004, Nature, 430, 181
Guaita, L. et al. 2010, ApJ, 714, 255
Hayes, M. et al. 2010a, Nature, 464, 562
Hayes, M., Schaerer, D., & Östlin, G. 2010b, A&A, 509, L5
Heavens, A., Panter, B., Jimenez, R., & Dunlop, J. 2004, Nature, 428, 625
Henriques, B. M. B., White, S. D. M., Lemson, G., Thomas, P. A., Guo, Q., Marleau, G.-D., & Overzier, R. A. 2012, MNRAS, 421, 2904
Ilbert, O. et al. 2009, ApJ, 690, 1236
Kauffmann, G., Colberg, J. M., Diaferio, A., & White, S. D. M. 1999, MNRAS, 303, 188
Kauffmann, G. et al. 2003a, MNRAS, 341, 33
—. 2003b, MNRAS, 341, 54
Kauffmann, G., White, S. D. M., & Guiderdoni, B. 1993, MNRAS, 264, 201
Klypin, A., Kravtsov, A. V., Valenzuela, O., & Prada, F. 1999, ApJ, 522, 82
Kodaira, K. et al. 2003, PASJ, 55, L17
Komatsu, E. et al. 2011, ApJS, 192, 18
Kravtsov, A. V., Gnedin, O. Y., & Klypin, A. A. 2004, ApJ, 609, 482
Kriek, M. et al. 2010, ApJ, 722, L64
—. 2008, ApJ, 677, 219
—. 2006, ApJ, 649, L71
Kriek, M., van Dokkum, P. G., Whitaker, K. E., Labbé, I., Franx, M., & Brammer, G. B. 2011, ApJ, 743, 168
Kroupa, P. 2001, MNRAS, 322, 231
Kümmel, M., Walsh, J. R., Pirzkal, N., Kuntschner, H., & Pasquali, A. 2009, PASP, 121, 59
Lacey, C., & Cole, S. 1993, MNRAS, 262, 627
Lara-López, M. A. et al. 2011, PASP, 123, 252
Larson, R. B. 1974, MNRAS, 166, 585
Le Fèvre, O. et al. 2000, MNRAS, 311, 565
Leauthaud, A. et al. 2012, ApJ, 744, 159
Lee, J. C. et al. 2012, ArXiv e-prints
López-Sanjuan, C., Balcells, M., Pérez-González, P. G., Barro, G., García-Dabó, C. E., Gallego, J., & Zamorano, J. 2009, A&A, 501, 505
Lotz, J. M. et al. 2008, ApJ, 672, 177
Lutz, D. et al. 2011, A&A, 532, A90
Ly, C., Lee, J. C., Dale, D. A., Momcheva, I., Salim, S., Staudaher, S., Moore, C. A., & Finn, R. 2011, ApJ, 726, 109
Ly, C. et al. 2007, ApJ, 657, 738
Maraston, C. 2005, MNRAS, 362, 799
Marchesini, D., van Dokkum, P. G., Förster Schreiber, N. M., Franx, M., Labbé, I., & Wuyts, S. 2009, ApJ, 701, 1765
McCarthy, P. J. et al. 2004, ApJ, 614, L9
Miley, G. K. et al. 2006, ApJ, 650, L29
Moles, M. et al. 2008, AJ, 136, 1325
Muzzin, A. et al. 2012, ApJ, 746, 188
Newman, A. B., Ellis, R. S., Treu, T., & Bundy, K. 2010, ApJ, 717, L103
Nilsson, K. K., Tapken, C., Møller, P., Freudling, W., Fynbo, J. P. U., Meisenheimer, K., Laursen, P., & Östlin, G. 2009, A&A, 498, 13
Oliver, S. J. et al. 2010, A&A, 518, L21
Ouchi, M. et al. 2004, ApJ, 611, 660
Pérez-González, P. G., Gil de Paz, A., Zamorano, J., Gallego, J., Alonso-Herrero, A., & Aragón-Salamanca, A. 2003, MNRAS, 338, 525
Pérez-González, P. G. et al. 2005, ApJ, 630, 82
—. 2008, ApJ, 675, 234
Papovich, C., Dickinson, M., & Ferguson, H. C. 2001, ApJ, 559, 620
Papovich, C. et al. 2006, ApJ, 640, 92
Percival, W. J. et al. 2001, MNRAS, 327, 1297
—. 2010, MNRAS, 401, 2148
Pforr, J., Maraston, C., & Tonini, C. 2012, MNRAS, 2944
Pirzkal, N. et al. 2009, ApJ, 695, 1591
—. 2004, ApJS, 154, 501
Reddy, N. A., Erb, D. K., Steidel, C. C., Shapley, A. E., Adelberger, K. L., & Pettini, M. 2005, ApJ, 633, 748
Reddy, N. A., Steidel, C. C., Erb, D. K., Shapley, A. E., & Pettini, M. 2006, ApJ, 653, 1004
Renzini, A. 2006, ARA&A, 44, 141
Ricciardelli, E., & Franceschini, A. 2010, A&A, 518, A14
Rix, H.-W. et al. 2004, ApJS, 152, 163
Saracco, P. et al. 2005, MNRAS, 357, L40
Scoville, N. et al. 2007, ApJS, 172, 150
Searle, L., & Zinn, R. 1978, ApJ, 225, 357
Shioya, Y. et al. 2008, ApJS, 175, 128
Sobral, D. et al. 2009, MNRAS, 398, 75
Sobral, D., Best, P. N., Matsuda, Y., Smail, I., Geach, J. E., & Cirasuolo, M. 2012, MNRAS, 420, 1926
Somerville, R. S., Hopkins, P. F., Cox, T. J., Robertson, B. E., & Hernquist, L. 2008, MNRAS, 391, 481

Somerville, R. S., & Primack, J. R. 1999, MNRAS, 310, 1087
Spergel, D. N. et al. 2007, ApJS, 170, 377
Spinrad, H., Dey, A., Stern, D., Dunlop, J., Peacock, J., Jimenez, R., & Windhorst, R. 1997, ApJ, 484, 581
Springel, V. et al. 2005, Nature, 435, 629
Takahashi, M. I. et al. 2007, ApJS, 172, 456
Teplitz, H. I., Malkan, M., & McLean, I. S. 1998, ApJ, 506, 519
Toomre, A., & Toomre, J. 1972, ApJ, 178, 623
Trager, S. C., Faber, S. M., Worthey, G., & González, J. J. 2000a, AJ, 120, 165
—. 2000b, AJ, 119, 1645
van Dokkum, P. G. 2005, AJ, 130, 2647
van Dokkum, P. G., Franx, M., Fabricant, D., Kelson, D. D., & Illingworth, G. D. 1999, ApJ, 520, L95
Vazdekis, A., Peletier, R. F., Beckman, J. E., & Casuso, E. 1997, ApJS, 111, 203
Villar, V., Gallego, J., Pérez-González, P. G., Pascual, S., Noeske, K., Koo, D. C., Barro, G., & Zamorano, J. 2008, ApJ, 677, 169
Whitaker, K. E. et al. 2011, ApJ, 735, 86
Willis, J. P., & Courbin, F. 2005, MNRAS, 357, 1348
Wirth, G. D. et al. 2004, AJ, 127, 3121
Wolf, C., Dye, S., Kleinheinrich, M., Meisenheimer, K., Rix, H.-W., & Wisotzki, L. 2001, A&A, 377, 442
Wolf, C. et al. 2004, A&A, 421, 913
Wolf, C., Wisotzki, L., Borch, A., Dye, S., Kleinheinrich, M., & Meisenheimer, K. 2003, A&A, 408, 499
Worthey, G. 1994, ApJS, 95, 107
Worthey, G., Faber, S. M., Gonzalez, J. J., & Burstein, D. 1994, ApJS, 94, 687
Yan, L., McCarthy, P. J., Weymann, R. J., Malkan, M. A., Teplitz, H. I., Storrie-Lombardi, L. J., Smith, M., & Dressler, A. 2000, AJ, 120, 575